



12-2001

## **A sub-scale investigation of automobile drag and lift interference in a 3/4- open jet wind tunnel**

Jeffrey Michael Hoffman

Follow this and additional works at: [https://trace.tennessee.edu/utk\\_gradthes](https://trace.tennessee.edu/utk_gradthes)

---

### **Recommended Citation**

Hoffman, Jeffrey Michael, "A sub-scale investigation of automobile drag and lift interference in a 3/4- open jet wind tunnel. " Master's Thesis, University of Tennessee, 2001.  
[https://trace.tennessee.edu/utk\\_gradthes/9640](https://trace.tennessee.edu/utk_gradthes/9640)

This Thesis is brought to you for free and open access by the Graduate School at TRACE: Tennessee Research and Creative Exchange. It has been accepted for inclusion in Masters Theses by an authorized administrator of TRACE: Tennessee Research and Creative Exchange. For more information, please contact [trace@utk.edu](mailto:trace@utk.edu).

To the Graduate Council:

I am submitting herewith a thesis written by Jeffrey Michael Hoffman entitled "A sub-scale investigation of automobile drag and lift interference in a 3/4- open jet wind tunnel." I have examined the final electronic copy of this thesis for form and content and recommend that it be accepted in partial fulfillment of the requirements for the degree of Master of Science, with a major in Mechanical Engineering.

Ahmad Vakili, Major Professor

We have read this thesis and recommend its acceptance:

Charles C. Limbaugh, Frank S. Collins

Accepted for the Council:

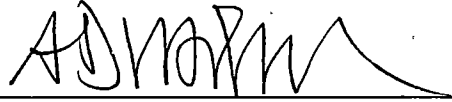
Carolyn R. Hodges

Vice Provost and Dean of the Graduate School

(Original signatures are on file with official student records.)

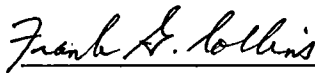
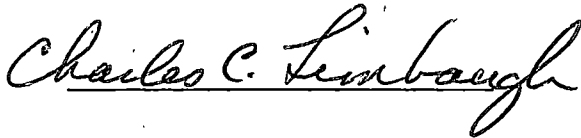
To the Graduate Council:

I am submitting herewith a thesis written by Jeffrey Michael Hoffman entitled "A Sub-Scale Investigation of Automobile Drag and Lift Interference in a  $\frac{3}{4}$ -Open Jet Wind Tunnel." I have examined the final paper copy of this thesis for form and content and recommend that it be accepted in partial fulfillment of the requirements for the degree of Master of Science, with a major in Mechanical Engineering.

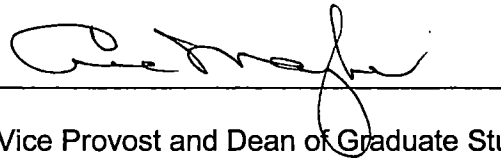


Ahmad Vakili, Major Professor

We have read this thesis  
and recommend its acceptance:



Accepted for the Council:



Vice Provost and Dean of Graduate Studies

A SUB-SCALE INVESTIGATION OF AUTOMOBILE DRAG AND  
LIFT INTERFERENCE IN A  $\frac{3}{4}$ - OPEN JET WIND TUNNEL

A Thesis  
Presented for the  
Master of Science  
Degree  
The University of Tennessee, Knoxville

Jeffrey Michael Hoffman  
December 2001

Copyright © Jeffrey Michael Hoffman, 2001  
All rights reserved

## Acknowledgements

I am indebted to the many individuals and organizations that have contributed to this work. Jack Williams and Stan Wallis of Ford Motor Company assisted in the data analysis and offered their valuable insight, both of which are sincerely appreciated. I also thank them for their permission to use this work for my thesis.

I also thank Dr. Ahmad Vakili, Dr. Charles C. Limbaugh, and Dr. Frank Collins, for serving on my committee, and for reviewing the manuscript. I have truly enjoyed interacting with and learning from these individuals, and value their participation in my education at UTSI. My thanks also go to Dr. Steve Arnette, who has provided friendship and professional direction—in addition to a thorough review of the manuscript.

I am indebted to my wife, Kerry, for her steady encouragement while I worked towards completing this degree. Her undying support was the key to my sustained effort. In addition, the enduring support of my family and friends made completing this degree possible. Finally, I thank my daughter, Grace, for entering my life near the end of this journey—your birth makes completing this degree that much sweeter.

## Abstract

The motivation for this study comes from the fact that aerodynamic interference is present in all wind tunnels. Here, aerodynamic "interference" is taken to be the deviation between the true result—which can only be estimated—and the actual result obtained from the wind tunnel. Because interference effects give rise to errors in wind tunnel simulation, they are an impediment to aerodynamic correlation of any new wind tunnel. Correction methods for interference effects have been most thoroughly investigated and, as a result, are best understood for solid wall test sections. Unfortunately, solid wall wind tunnels devoted to full-scale automotive testing have to be very large (test section areas of approximately 500 ft<sup>2</sup> or larger) to hold the simulation error to correctable levels. For open jet test sections, which have traditionally been the choice of the European community for aerodynamic testing, interference effects have never truly been quantified. Only in recent years have open jet test sections become a popular choice for aerodynamic test facilities in North America. The cumulative result is that open jet aerodynamic interference is poorly understood.

# Table of Contents

Chapter 1 Summary .....	1
Chapter 2 Review of Previous Work.....	6
Chapter 3 Current Approach to Developing Lift and Drag Corrections .....	9
Regression Methodology.....	9
Blockage Ratio (%).....	10
Length/ $\sqrt{\text{Frontal area}}$ .....	11
$\sqrt{\text{Frontal area}}$ / Distance from nozzle .....	11
$\sqrt{\text{Frontal area}}$ / Rear bumper to collector.....	12
Aspect Ratio .....	14
Vehicle height / nozzle height.....	14
Chapter 4 Experimental Procedure .....	16
Empty Tunnel Flow Characteristics .....	16
Model Geometries .....	21
Open Jet Wind Tunnel Configuration .....	27
Adaptive Wall Wind Tunnel Configuration.....	30
Dynamic pressure measurement (Adaptive wall).....	32
Adaptive Wall Measurements.....	33
Force Balance .....	34
Methods of Open Jet Dynamic Pressure Measurement .....	37
Ground Effects.....	40
Estimate of Experimental Error .....	46
Chapter 5. Presentation of Experimental Results .....	48
Open Jet: MIRA Models .....	48
Open Jet: SUV Models.....	53



Adaptive Wall: MIRA and SUV Models .....	56
Chapter 6 Results of Regression Analysis .....	67
Drag correlation .....	68
Lift correlation .....	78
Application of Correction to Validation Model.....	86
Chapter 7 Conclusion .....	88
Bibliography .....	91
Appendix.....	94
Appendix A Tabulated numerical values for selected plots.....	95
Plotted values of $C_D$ and $C_L$ .....	95
Model blockage .....	96
Vita.....	98

## List of Tables

Table 1. Measurement characteristics of employed force balance.....	34
Table 2. Independent variables used in drag correlation.....	69
Table 3. Prediction accuracy of drag correlation equation using Equation 4.....	74
Table 4. Independent variables used in drag correlation.....	75
Table 5. Prediction accuracy of drag correlation equation using Equation 5.....	77
Table 6. Potential variables used in lift correlation.....	78
Table 7. Accuracy of lift correlation equation with all variables (Floating intercept).....	82
Table 8. Potential variables used in lift correlation.....	82
Table 9. Prediction accuracy of lift correlation equation with all variables.....	85
Table 10. Correlation accuracy for predicting $C_D$ and $C_L$ for validation model ("floating intercept" using all independent variables).....	86
Table 11. Correlation accuracy for predicting $C_D$ and $C_L$ for validation model ("zero intercept" using all independent variables).....	87
Table 12. Numerical values for open jet, adaptive wall, and University of Maryland data.....	95
Table 13. Model blockage for all wind tunnels used in study.....	96
Table 14. Dimensionless parameters for models.....	97

## List of Figures

Figure 1. Model position influence on aerodynamic drag.....	13
Figure 2. Model position influence on aerodynamic lift .....	13
Figure 3. Axial static pressure distribution in the empty test section.....	17
Figure 4. Velocity boundary layer profiles at balance center (20 m/s and 60 m/s). .....	18
Figure 5. Fluctuating pressure, $C_{P,RMS}$ .....	20
Figure 6. MIRA Model geometry with tabulated dimensions (dimensions in inches).....	22
Figure 7. SUV Model geometry with tabulated dimensions (dimensions in inches). .....	23
Figure 8. MIRA models shown with various modification blocks.....	24
Figure 9. The Small SUV and Large SUV (Before wheels were removed).....	24
Figure 10. Back end of validation model. ....	25
Figure 11. $C_D$ and $C_L$ as a function of Reynolds number (Fastback model). .....	26
Figure 12. Overall open jet wind tunnel configuration. ....	28
Figure 13. Open jet wind tunnel (Dimensions in inches).....	28
Figure 14. Image of scale model setup showing open jet plenum with inset collector flaps.....	29
Figure 15. Photograph of adaptive wall test section setup.....	31
Figure 16. Diagram of adaptive wall test section.....	31
Figure 17. Adaptive wall dynamic pressure calibration. ....	32
Figure 18. Image of load cell arrangement (balance is tilted on its side).....	35
Figure 19. Double-exposure photograph showing how balance mounts inside model.....	36
Figure 20. Typical load cell calibration curve. ....	37
Figure 21. Diagram of plenum pressure taps placement in open jet model.....	38
Figure 22. Open jet dynamic pressure calibration.....	39
Figure 23. $(C_D - C_{D,0})/C_{D,0}$ for Q measurement methods (MIRA Pickup).....	41
Figure 24. $(C_D - C_{D,0})/C_{D,0}$ for Q measurement methods (MIRA Fastback).....	41

Figure 25. $(C_D - C_{D,0})/C_{D,0}$ for Q measurement methods (MIRA Squareback).....	42
Figure 26. $C_D$ as a function of ground clearance.....	44
Figure 27. $C_L$ as a function of ground clearance.....	44
Figure 28. Comparison of $C_L$ dependence on ground clearance (MIRA 15 fastback).....	45
Figure 29. Example uncertainty calculation on drag coefficient.....	46
Figure 30. $C_D$ values for the MIRA models (Open jet and adaptive wall).....	49
Figure 31. $C_D$ values for the MIRA models (University of Maryland and adaptive wall).....	50
Figure 32. $C_L$ values for the MIRA models (Open jet and adaptive wall).....	52
Figure 33. $C_L$ values for the MIRA models (University of Maryland and adaptive wall).....	53
Figure 34. $C_D$ values for the SUV models.....	54
Figure 35. $C_D$ values for the SUV models (University of Maryland and adaptive wall).....	55
Figure 36. $C_L$ values for the SUV models.....	56
Figure 37. MIRA 11 Fastback.....	57
Figure 38. MIRA 11 Squareback.....	57
Figure 39. MIRA 11 Pickup.....	58
Figure 40. MIRA 15 Fastback.....	58
Figure 41. MIRA 15 Squareback.....	59
Figure 42. MIRA 15 Pickup.....	59
Figure 43. MIRA 15 Validation Model (Fastback with spoiler).....	60
Figure 44. MIRA 20 Fastback.....	60
Figure 45. MIRA 20 Squareback.....	61
Figure 46. MIRA 20 Pickup.....	61
Figure 47. MIRA 25 Pickup.....	62
Figure 48. Small SUV (Low height).....	62
Figure 49. Small SUV (Medium height).....	63
Figure 50. Small SUV (High height).....	63
Figure 51. Large SUV (Low height).....	64

Figure 52. Large SUV (Medium height).....	64
Figure 53. Large SUV (High height).....	65
Figure 54. Errors from combinations of correlation variables ("Floating Intercept", Drag).....	71
Figure 55. Errors from combinations of the correlation variables ("Zero Intercept", Drag).....	76
Figure 56. Errors from combinations of correlation variables ("Floating Intercept", Lift).....	80
Figure 57. Errors from combinations of correlation variables ("Zero Intercept", Lift).....	84

## List of Symbols

$C_D$	Drag Coefficient
$C_{D,0}$	Reference drag coefficient
$c_i$	Weighting coefficient in a correction equation
$C_L$	Lift Coefficient
$Q$	Dynamic pressure
$R$	Edge radius
$Re$	Reynolds number
$W$	Width
$y$	Vehicle body height
$\Delta C_D$	Change in drag coefficient
$\Delta C_L$	Change in lift coefficient
$\Delta P$	Differential pressure
$\eta$	Uncertainty
$\alpha_i$	Dimensionless parameter used in correction equation

### **Abbreviations**

AR	Aspect ratio
AW	Adaptive wall
DTF	Driveability Test Facility
FA	Frontal area
FB	Fastback
HOL	Hood Length
L1	Distance from vehicle trailing edge to balance center
LgSUV	Large Sport Utility Vehicle
MIRA	Motor Industry Research Association

mph	miles per hour
Nd: YAG	Neodymium: Yttrium Aluminum Garnet
OJ	Open jet
PIV	Particle Image Velocimetry
PU	Pickup
SB	Squareback
SmSUV	Small Sport Utility Vehicle
SUV	Sport Utility Vehicle
UMD	University of Maryland
W/H	Width-to-height ratio
WT8	Wind Tunnel 8

# Chapter 1

## Summary

The motivation for this study comes from the fact that aerodynamic interference is present in all wind tunnels. Here, aerodynamic "interference" is taken to be the deviation between the true result—which can only be estimated—and the actual result obtained from the wind tunnel. Because interference effects give rise to errors in wind tunnel simulation, they are an impediment to aerodynamic correlation of any new wind tunnel. Correction methods for interference effects have been most thoroughly investigated and, as a result, are best understood for solid wall test sections. Unfortunately, solid wall wind tunnels devoted to full-scale automotive testing have to be very large (test section areas of approximately 500 ft<sup>2</sup> or larger) to hold the simulation error to correctable levels. In automotive applications, an open jet wind tunnel is a wind tunnel where the test section is three-fourths open and a level floor represents the road (SAE SP-1465, 1999). A plenum contains the test section in the current study, and is a typical feature of open jet wind tunnels. For open jet test sections, which have traditionally been the choice of the European community for aerodynamic testing, interference effects have been difficult to quantify. Only in recent years have open jet test sections become a popular choice for aerodynamic test facilities in North America. The cumulative result is that open jet aerodynamic interference is poorly understood.



There are four types of test sections commonly used in automotive wind tunnel testing: closed wall, slotted wall, open jet, and adaptive wall. Each type of test section has advantages and disadvantages associated with its use. A closed wall test section has rigid walls that cannot be moved. Of the four test section types mentioned, the closed wall type exhibits the worst test section interference. However, it is the most common type of test section because of the traditional role it has played in aerospace research. Its popularity makes it a common subject of interference research, providing a wider base of knowledge for closed test section interference. Another type of test section is the open jet—more specifically the three-quarter open jet. This typically employs a fixed ground plane in front of a three-sided jet, which is often placed in a larger enclosure called a plenum. The current research focuses on interference in this type of test section. A third type of test section is the slotted wall—a compromise between a closed wall and open jet test section in that the streamlines in the flow are given more freedom to diverge at the side and top walls of the test section (Hoffman et al., 2001). The complex nature of the boundary conditions makes a theoretical correction scheme difficult to create. A fourth type of test section is the adaptive wall, which is utilized in the current investigation to yield interference-free data. By shaping the walls to create the streamline shape that would occur in an interference-free environment, the adaptive wall test section imparts no interference effects on the model. A later section provides additional discussion of the adaptive wall concept.

In addition to the large capital cost for a solid wall wind tunnel sufficiently large for aerodynamic testing, there are other compelling reasons to choose an open jet configuration. The low background noise level required for acoustic testing requires an

open jet test section. Due to the absence of boundary layer noise radiating from the walls of the test section, open jet wind tunnels can be designed to be substantially quieter than those with solid wall test sections. In a previous study, a sub-scale experimental program was carried out to investigate the advantages of using a slotted wall test section insert for improved aerodynamic simulation relative to the open jet (Hoffman et al., 2001). The program showed no increase in aerodynamic simulation fidelity for a wind tunnel with both open jet and slotted wall test capabilities. This coupled with (i) the operational penalty associated with interchangeable test sections, i.e. separate acoustic and aerodynamic test sections, and (ii) the acoustic penalty associated with a slotted wall relative to an open jet, (i.e. the open jet is substantially quieter than the slotted wall)—resulted in the conclusion that it is advantageous to have an exclusively open jet facility.

Because aerodynamic interference is poorly understood for open jet test sections, the current study was carried out to provide a thorough investigation of aerodynamic simulation in an open jet wind tunnel. The specific objectives of the project were:

- to carry out a sub-scale experimental investigation of aerodynamic simulation error present in open jet wind tunnels. Simulation errors were obtained by direct comparison to measurements obtained in an adaptive wall wind tunnel, and
- to use multivariate linear regression on the resulting dataset to develop lift and drag corrections that remove to the extent possible simulation errors attributable to open jet interference.

In summary, the objective was to establish correlations between  $\frac{3}{4}$ -open jet data obtained in a 1:11-scale model and interference free data. The open jet experiments were carried out in a 1/11-scale model of an existing full-scale open jet facility, namely Wind Tunnel 8 of the Ford/Sverdrup Driveability Test Facility in Allen Park, Michigan. This wind tunnel has a 200 ft<sup>2</sup> nozzle area and has a maximum test section speed of 150 mph. The facility has aerodynamic, powertrain, acoustic, and thermal test capabilities.

To maximize its applicability, the experiments were carried out for an ensemble of models representative of a full range of vehicle shapes and blockages. Reference data were obtained by testing the same models in an adaptive wall wind tunnel, using the same force balance as employed in the open jet experiments. The adaptive wall test section has been shown to be free of aerodynamic interference for vehicle blockages approaching 30%, so the adaptive wall results were adopted as "error free" reference data for the current study. Test section speed measurement was accomplished using the "nozzle method" of dynamic pressure measurement, which uses the differential pressure across the contraction section of the wind tunnel. This process is described in detail in a later section.

The subscale facility employed in the current study is part of Sverdrup Technology, Inc.'s Aerodynamic Laboratory in Tullahoma, Tennessee. It is an open-inlet wind tunnel utilizing a 30 horsepower axial fan. The wind tunnel can be reconfigured to replicate a scaled-down version of virtually any full-scale wind tunnel, including those with open jet, closed wall, slotted wall, and adaptive wall test sections. The wind tunnel is used for applied research and development activities, typically in support of a facility design.

The employed vehicles were based on the Motor Industry Research Association (MIRA) vehicle geometry, which is a generic vehicle intended for use in test section interference studies. The model blockages for the MIRA models can be derived from their names. For example, the MIRA 15 has a 15% blockage in the open jet test section, which has a cross-sectional area of  $12'' \times 20'' = 240 \text{ in}^2$ . Because only the model backlight angle was changed to achieve a different model type (i.e. fastback, squareback, or pickup), the frontal area did not change for a given model. For example, the MIRA 11 fastback has the same frontal area as the MIRA 11 squareback. SUV and MIRA model blockages in all of the employed wind tunnels are presented in Appendix A in Table 13.

This thesis summarizes the experiments that were performed and the process by which the correction equations were obtained. The final results indicate that:

1. Vehicle blockage and the vehicle's location in the test section are important variables for correcting aerodynamic drag interference errors.
2. Increasing vehicle size (especially height) increases interference on lift measurements.

Although the results of this work will likely not be directly applicable to all open jet wind tunnels due to the multitude of potential configurations, they provide a solid foundation for developing a standing correction procedure suitable for use in the current open jet wind tunnel. The results highlight several key test variables that should be considered in interpreting aerodynamic force and moment measurements. Combining these results with full-scale correlation testing activities should provide a comprehensive data set with which to develop an aerodynamic correction methodology.

## Chapter 2

### Review of Previous Work

The current study quantifies the difference between open jet measurements and "interference-free" measurements, which is required to develop a data correction procedure for open jet wind tunnels. Previous work by Mercker carried out in Europe yielded a drag correction method intended for general use in open jet wind tunnels (Mercker et al., 1996). The study provides valuable insight into the physical mechanisms that govern open jet aerodynamic interference, but the resulting drag correction does not do a good job of correcting all open jet data sets to within acceptable limits. Specifically, application of Mercker's open jet correction to data obtained in a study performed by Hoffman did not successfully remove the interference effects (Hoffman et al., 2001). The current study is based on using a purely empirical method (linear regression) to determine the influence of several relevant independent variables on the total interference magnitude, whereas other methods have attempted to develop a semi-theoretical model with which to quantify interference effects.

Experiments were performed at the University of Maryland Glenn L. Martin Wind Tunnel to supplement the current experimental campaign. The University of Maryland wind tunnel employs a closed-wall test section with cross sectional area of 85.04 ft<sup>2</sup>, and has a maximum test section velocity of 230 mph. Unlike the other facilities used in the

current study, the University of Maryland wind tunnel has boundary control capability to minimize boundary layer thickness on the Test Section floor.

The University of Maryland experiments were conducted to verify the results of the adaptive wall tests. Because of the relatively small blockage ratio (all models were less than 0.5% blockage), the data truly approached a zero-blockage case, where interference effects are non-existent—the scenario simulated by the adaptive wall test section. Therefore, the University of Maryland tests were conducted to independently evaluate the interference-free coefficients.

Open jet corrections for automotive applications have taken several forms. The Society of Automotive Engineers formed a subcommittee to investigate such correction techniques due to their importance in the wind tunnel community. The results of their findings are presented in Aerodynamic Testing of Road Vehicles in Open Jet Wind Tunnels (SAE SP-1465, 1999). It references to an investigation employing mirror imaging and potential flow to estimate the boundary influences (Wuest, 1961). That study concluded that the three quarter open jet correction was much smaller than the closed jet correction. Further work by Mercker et al. identified four different open jet interference effects using small perturbation theory (Mercker et al., 1996 and 1997). That work characterizes the test section flow dynamics using theoretical models before applying a correction to experimental data, a sort of semi-theoretical approach. However, Hoffman et al. showed application of this correction scheme is not universally successful (Hoffman et al., 2001) at removing boundary influences from experimental data. Hackett et al. implement a pressure signature-based correction scheme in a

closed wall facility where axial static pressure distribution is measured along the test section walls, but the author knows of no attempt to apply the same technique to open jet test sections (Hackett et al., 1978). The distinguishing feature of the current investigation is that it relies entirely on empirical data to derive the correction scheme.

## Chapter 3

### Current Approach to Developing Lift and Drag Corrections

Correction equations for drag and lift were derived using multivariable linear regression. Employing such analysis assumes that the interference effects add linearly. This assumption greatly simplifies the governing aerodynamics, but makes implementing the resulting correction straightforward. The current work does not attempt to formulate a physical model of the aerodynamics governing open jet interference. The governing aerodynamics are complex, and have not yet been captured in a coherent theoretical model. Rather, the least squares method (described in detail below) was used to empirically determine weighting coefficients for each of the independent variables considered in the study. A complete explanation of the selected variables is presented in the next section.

#### **Regression Methodology**

In a typical implementation of the correction equation, adjustments are made to the open jet data based on the physical parameters of the model being tested. The general form of the drag and lift correction equations is:

$$C_{Corrected} = C_{Open\ Jet} + c_1\alpha_1 + c_2\alpha_2 + c_3\alpha_3 + \dots$$

**Equation 1**

where  $C$  is an aerodynamic coefficient ( $C_D$  or  $C_L$ )

$c_i$  is a weighting coefficient

$\alpha_i$  is a dimensionless variable



The weighting coefficients in Equation 1 are determined using the least squares method for multiple variables.

The variables used in the linear regression were selected based on previous experience (primarily from publications on open jet corrections) and engineering judgment (Mercker et al., 1996; Williams et al., 1999). All independent variables used in this study were cast in dimensionless form. Obviously, model blockage is a principle factor in determining open jet interference. While this captures gross effects of the model size, it does not include other effects that can significantly alter the interference, such as model geometry and proximity to wind tunnel boundaries. Therefore, variables were selected that characterized not only the model geometry, but also the model's position in the wind tunnel.

### **Blockage Ratio (%)**

In open jet testing, models with large frontal areas relative to the nozzle cross section deflect the jet boundary and alter the aerodynamic lift and drag on the vehicle. How these flowfield alterations influence the aerodynamic lift and drag is difficult—in fact, currently impossible—to predict theoretically. However, it is well established that interference effects generally increase with increasing blockage ratio. The vehicles tested had blockage ratios ranging from 11% to 25%. Translating these results to the open jet facility employed in the current study, this range of blockages would include full-scale vehicles with frontal areas as large as 50ft<sup>2</sup>.

### **Length/ $\sqrt{\text{Frontal area}}$**

Large blockage ratios do not necessarily indicate large drag coefficients. For example, a long model with large projected frontal area can have a relatively low drag coefficient if it is reasonably faired. The parameter defined by model length over the square root of frontal area is included to refine the model geometry characterization and allow for larger vehicles with faired bodies. This dimensionless variable was adopted from Mercker's open jet correction work, which captures the three-dimensional geometry of the model.

### **$\sqrt{\text{Frontal area}} / \text{Distance from nozzle}$**

A central reason for including a model position parameter is that aerodynamic forces are not independent of model scale when taken in an open jet test section. In an environment free of boundary influences, scale does not affect aerodynamic coefficients. However, in an open jet, similarly shaped models of different scale are subjected to different levels of "collector" or "nozzle" interference effects. By considering the model's size relative to the test section, the correlation of the current study attempts to capture these effects. Note that the parameter is defined such that, as the clearance between the nozzle exit and the model approaches infinity, the parameter goes to zero. By this line of reasoning, this definition is physically intuitive.

A previous subscale study performed by Hoffman revealed that axial model position in the wind tunnel influences aerodynamic model drag (Hoffman et al., 2001). As illustrated in Figure 1, a repeat of this experiment in the current program confirmed this dependence. In this experiment, the  $C_D$  and  $C_L$  behavior of two models was observed when the model was placed at different positions along the test section length. In Figure

1 and Figure 2, "balance center" is the location of the force measurement balance in the full-scale facility, and where the location of the balance for remaining tests. The two models were a fastback and a Sport Utility Vehicle (SUV). The trend of a slight adverse pressure gradient resulting in increasing static pressure at the base of the model as it is positioned further downstream (closer to the diffuser downstream of the test section) is consistent with the results of a study in the Lockheed Low Speed Wind Tunnel (Garry et al., 1994).

Figure 2 presents the lift results from the same experiments, highlighting that the lift coefficient is likewise strongly affected by model proximity to the ends of the test section. Note that the data points on the plot represent the axial location of the balance center for the measurements. In general, the results of Figures 1 and 2 show that the drag coefficient decreases and the lift coefficient increases as the model is positioned further downstream from the nozzle exit plane. Because model proximity to the downstream end of the test section affects both drag and lift measurements, it must be characterized to fully capture aerodynamic influence near the collector and nozzle. This is accomplished by including the parameter defined as the square root of frontal area divided by the distance from the nozzle to the model front bumper.

#### **$\sqrt{\text{Frontal area} / \text{Rear bumper to collector}}$**

Similar to the previous parameter, the distance from the model trailing edge to the collector leading edge was defined to capture "collector" effects, which are nominally associated with adverse static pressure gradients in the vicinity of the collector. Again, as the distance between the model and the collector increases (which would cause this parameter to become less relevant), the ratio decreases.

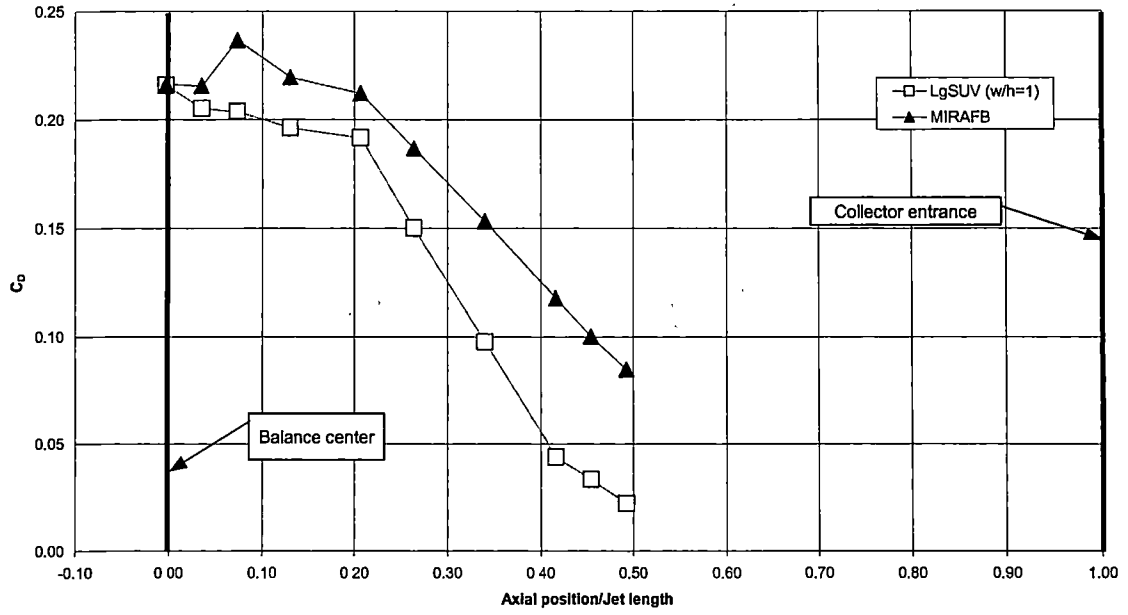


Figure 1. Model position influence on aerodynamic drag.

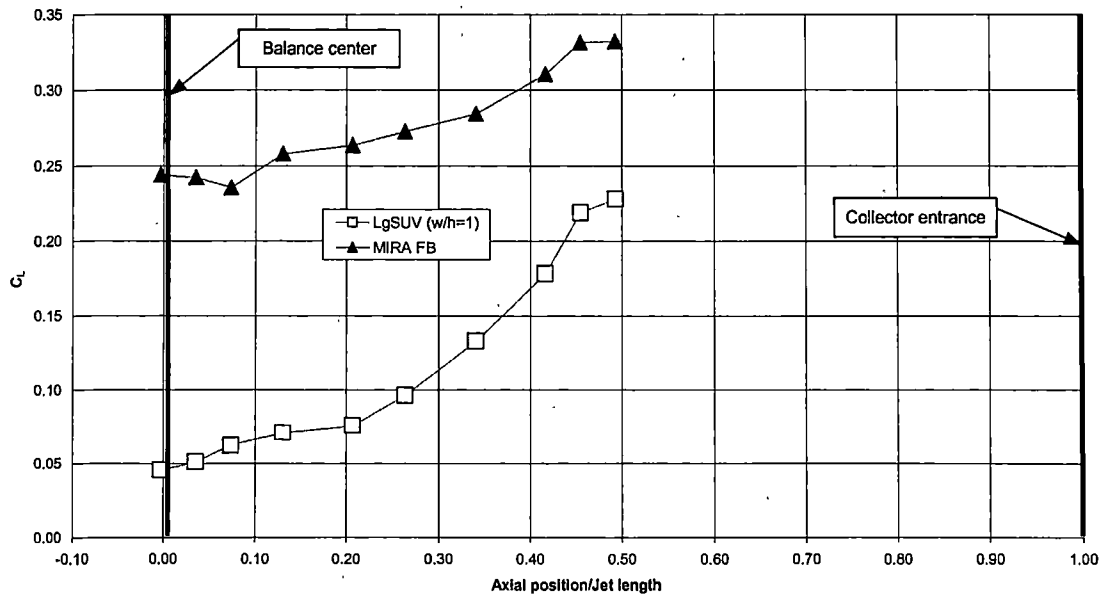


Figure 2. Model position influence on aerodynamic lift

### **Aspect Ratio**

Williams showed that vehicle aspect ratio affects drag coefficient (Williams et al., 1999). While this ratio (defined here to be the ratio of width/height) is fixed for all of the MIRA models used in this study, several "Sport Utility Vehicle" (SUV) models whose dimensions were based on the Ford Explorer and Expedition were also used. Therefore, this parameter is included to capture any aerodynamic trends attributable to changes in aspect ratio. Each of the SUV models was equipped with removable modification blocks that could be used to change the model aspect ratio by increasing the model height (at constant width). A complete definition of the geometry of the various models is presented below.

### **Vehicle height / nozzle height**

This parameter is included to characterize the vehicle's tendency to deflect the jet exiting the nozzle. Since larger models will tend to be taller, they will therefore approach the top boundary of the jet core. As a result, a model height-dependent aspect of the aerodynamic interference is possible. This parameter captures the height changes of the variable-scale MIRA models, which aids the correlation by further defining the model shapes. Including a parameter to characterize vehicle width to nozzle width would not add significant value because typical vehicle aspect ratios are near unity—meaning that vehicle width changes almost proportionately to vehicle height. In extreme cases, vehicle height is large relative to other parameters. It is in these cases that this parameter is expected to be particularly effective at quantifying the interference effects.

Other parameters could be used to characterize the vehicle and the test section aerodynamics. For example, a parameter that quantifies how "faired" a vehicle shape is

would be appropriate. Such a variable could take the vehicle's edge radii with respect to other lengths into consideration, including test section or vehicle dimensions. A study on the effect of leading-edge radii on the drag of a rectangular box showed that (for a given bus-like configuration) including rounded leading edge radii decreased drag coefficient by greater than 50%—a dramatic improvement in aerodynamic performance for a modest change in front-end geometry (Gilhaus, 1981). This supports the fact that gross passenger vehicle profiles have remained virtually unchanged for decades, but still benefit from further reductions in drag by the use of modest alterations to edge radii.

Such vehicle characterization parameters, while appropriate in vehicle design, were not included in the current study because they relate more to vehicle design than to test section interference. Moreover, the employed model set would reap little benefit from a parameter that quantifies how "faired" the vehicles are due to the fact that the same model was created at different scales (in the case of the MIRA models). In this case, that specific parameter would not vary from model to model—and would therefore offer little insight into the test section aerodynamics.

Potential variables were excluded from the regression analysis for two reasons: *i)* changes in the dimensionless variable did not change the measured coefficient, and *ii)* the dimensionless variable was constant—or near constant—for all tests. The first reason was substantiated through experiments (e.g. a test was conducted to determine if changing a variable affected the results). The rationale for the second reason was that if a variable were constant for all tests, it would not enhance the understanding of the Test Section interferences.

## Chapter 4

### Experimental Procedure

This chapter describes the experimental procedure. Detailed descriptions are presented of the empty tunnel flow characteristics, model geometries, wind tunnel configurations, and measurement techniques.

#### **Empty Tunnel Flow Characteristics**

Tests were performed to characterize empty tunnel flow in the current model. Because empty test section aerodynamics plays an important role in model interference, the results are critical to understanding the overall interference effects.

#### ***Axial Static Pressure Gradient***

A nonuniform static pressure distribution along the test section centerline will tend to "pull" the test vehicle in one direction, creating drag due only to the test section aerodynamics. This effect is commonly referred to as horizontal buoyancy. To quantify the magnitude of this pressure gradient, a pipe with static pressure taps was placed in the test section. The pipe was positioned on the spanwise centerline and extended axially. The thirty-two static taps on the pipe covered a region from the nozzle exit to the collector exit. The static pressure at each tap was measured and compared to the static pressure at the nozzle exit, and a pressure coefficient was calculated. A flat pressure coefficient distribution indicates that there is no pressure gradient—and therefore zero horizontal buoyancy effect. The results of this test are shown in Figure 3.

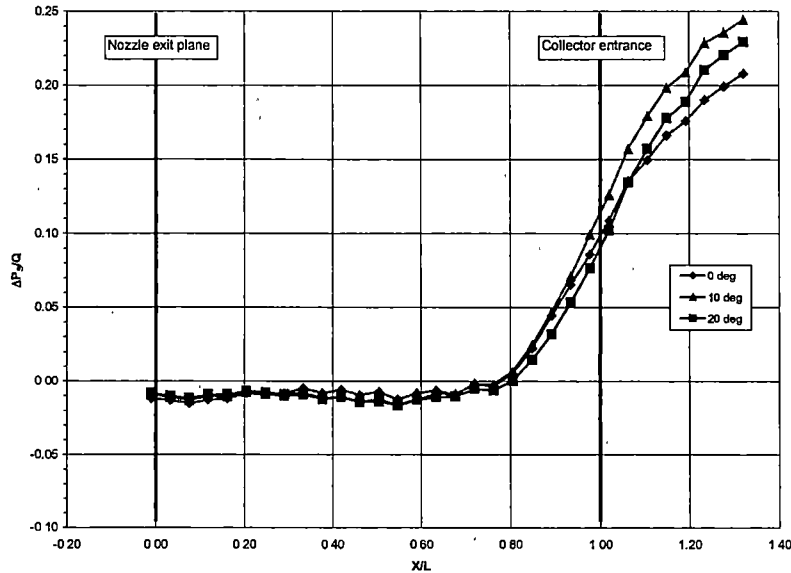


Figure 3. Axial static pressure distribution in the empty test section.

The collector consists of three flaps that guide the jet into the diffuser. Collector flap angle was defined to be the angle formed between the flow axis and the face of the collector flap. Three flap settings were tested:  $0^\circ$ ,  $10^\circ$ , and  $20^\circ$  relative to the flow direction. In Figure 3,  $X/L=0$  is at the nozzle exit and  $X/L=1$  is at the plane of the collector entrance. The data show that the pressure gradient in the test region is small, indicating that horizontal buoyancy effect will be proportionately small.

#### *Boundary Layer*

The empty tunnel boundary layer was measured using Particle Image Velocimetry (PIV) in the open jet test section. PIV instantaneously captures the movement of buoyant fog particles in the flow using an Nd:YAG laser and digital photography techniques. The result is a plane of two-dimensional velocity vectors indicating magnitude and direction of the flow. Over one hundred vector fields at the balance center were averaged to yield the velocity profiles shown in Figure 4.



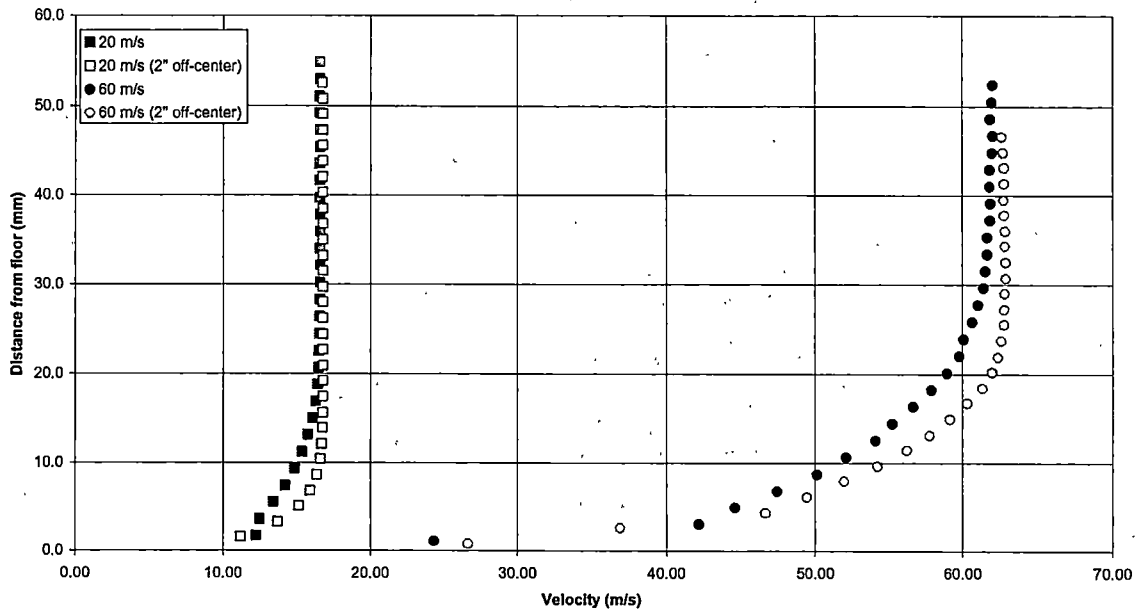


Figure 4. Velocity boundary layer profiles at balance center (20 m/s and 60 m/s).

It should be noted that the boundary layer thickness *increases* with increasing wind speed, which runs counter to the trend predicted by flat plate boundary layer theory. Several repeat runs of the experiment confirm that this is a characteristic of the boundary layer in the employed model. PIV measurements made at balance center axially, but at a different spanwise location (two inches left of tunnel centerline, when looking upstream) show the same trend, but with lower magnitudes of boundary layer thickness. This suggests complicated three-dimensional behavior near the floor. However, mean pitch flow angularity (less than one-half degree in both the boundary layer and in the mean flow) was not large enough to suggest strong vortical patterns that might adversely affect the pitch- and yaw-moment of the vehicle. While this boundary layer behavior is puzzling, it is not believed to influence the vehicle measurements because of the high ground clearance maintained in the tests.

Mean pitch flow angle may be extracted from the boundary layer results, as well. Using the PIV results, the mean pitch flow angle is found to be 0.5 degrees, pitching upward. While this is a relatively small flow angle, it will manifest in the model force data. Specifically, it will alter the lift and drag results by causing a component of the drag force to add to the lift component. Although considered a secondary effect, it will also affect model pitching moment.

### *Pressure Fluctuations*

The fluctuating component of static pressure was measured in the empty test section. Pressure fluctuations are a result of flow oscillations in the shear layer emerging from the open jet nozzle. The fluid emerging from the jet interacts with the quiescent plenum air and excites the flow, causing it to oscillate. If the frequency of this oscillation is near a naturally occurring acoustic mode in the circuit ducting, large pressure fluctuations in the test section result.

Fluctuating pressure measurements were acquired for a range of test section velocities, as shown in Figure 5.  $C_{P,RMS}$  is defined as the standard deviation of the pressure, divided by the mean dynamic pressure in the test section. The peak in fluctuation amplitude near 57 mph is evidence of a shear layer frequency that has excited another component of the wind tunnel ducting. This pressure fluctuation could contaminate the model force measurements by causing the model to fluctuate, as well. This slight fluctuation would most likely impose a frequency on the model data, not altering the mean value.

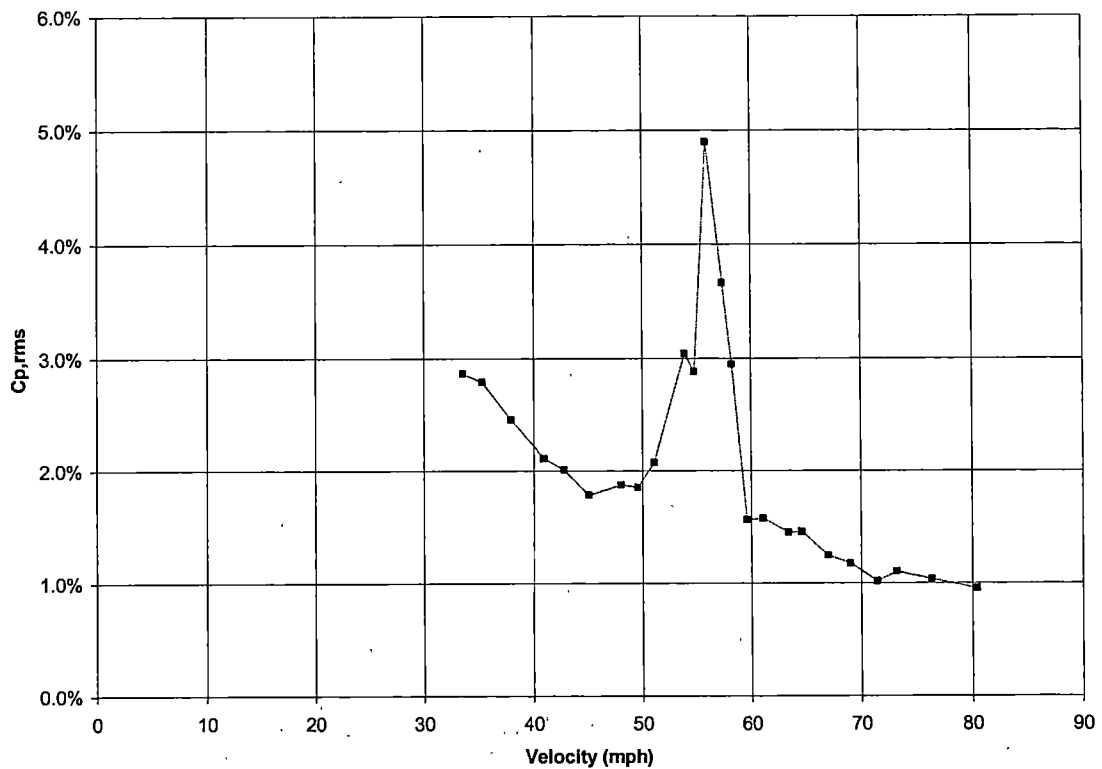


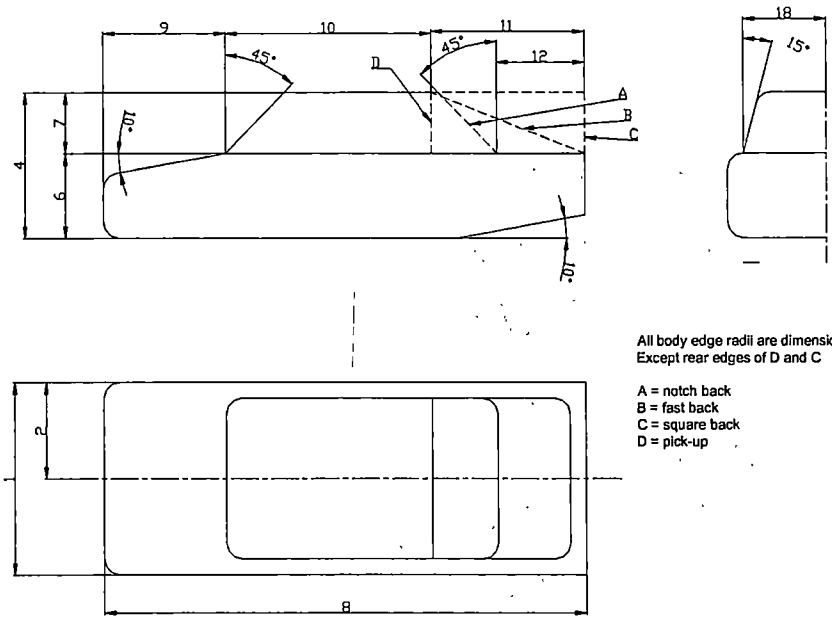
**Figure 5. Fluctuating pressure,  $C_{p,RMS}$**

For example, a model placed near the jet boundary will tend to deflect the jet more outward (away from centerline), be subjected to a non-uniform dynamic pressure distribution (because of being partially submerged in the shear layer), and may even experience interference from the plenum walls due to local acceleration. This illustrates the complex, three-dimensional aerodynamics of open jet testing, and makes apparent the need for high flow quality standards. Under ideal circumstances, the entire jet core is considered usable for aerodynamic testing. However, even in that circumstance, proximity to plenum walls and the collector will subject the model to pressure gradients that influence the final data.

## Model Geometries

Automobile models were created for use in the current work. The set contained a total of 18 models, consisting of two main model sets: MIRA (Motor Industry Research Association) vehicles, and SUV models. MIRA created a set of generic vehicle geometries for use in evaluating test section interference effects. The MIRA shapes used were the pickup, fastback, and squareback. Six SUV shapes were also used. These include two models, the small SUV and the large SUV—geometrically similar to the Ford Explorer and Expedition, respectively. Each of the SUV models has three modification blocks that can be used to change the height of the model, but not the width. These modification blocks vary the width-to-height ratio of the SUVs, with possible combinations of 0.85, 1.00, and 1.15. The dimensions of the MIRA vehicles are shown with a diagram of the cars in Figure 6. The SUV dimensions are shown in Figure 7. Figure 8 shows the MIRA models with the possible modification blocks, and Figure 9 shows the two SUV models.

High dimensional accuracy was critical to attaining the fidelity required for a reliable correlation. In addition, low model weight was desirable because of the employed balance's weight limit. For that reason, stereo lithography was chosen as the manufacturing technique for the models. This technique employs a laser to fuse polymer liquid into lightweight, accurate parts. Nominal accuracy of the manufacturing process is approximately 0.002 inch. This provides the required accuracy for the current tests. The models were hollow to further reduce their overall weight, with a honeycomb-like supporting structure inside for rigidity. An added benefit of using stereo lithography is that creating scale versions of the same model geometry is straightforward.

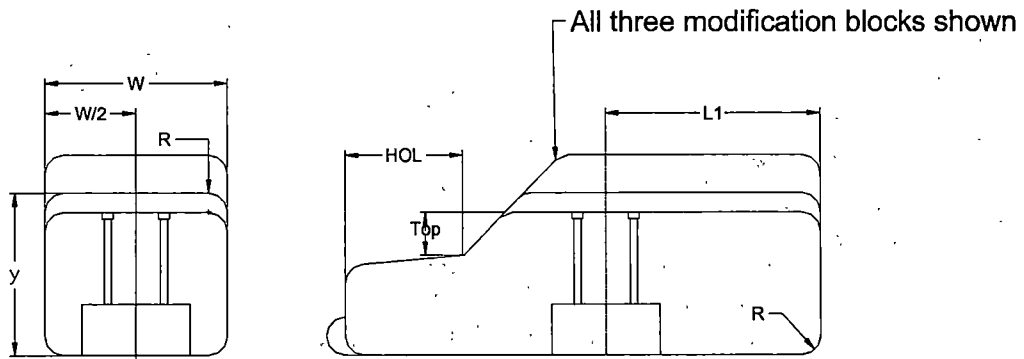


All body edge radii are dimension 19  
 Except rear edges of D and C

A = notch back  
 B = fast back  
 C = square back  
 D = pick-up

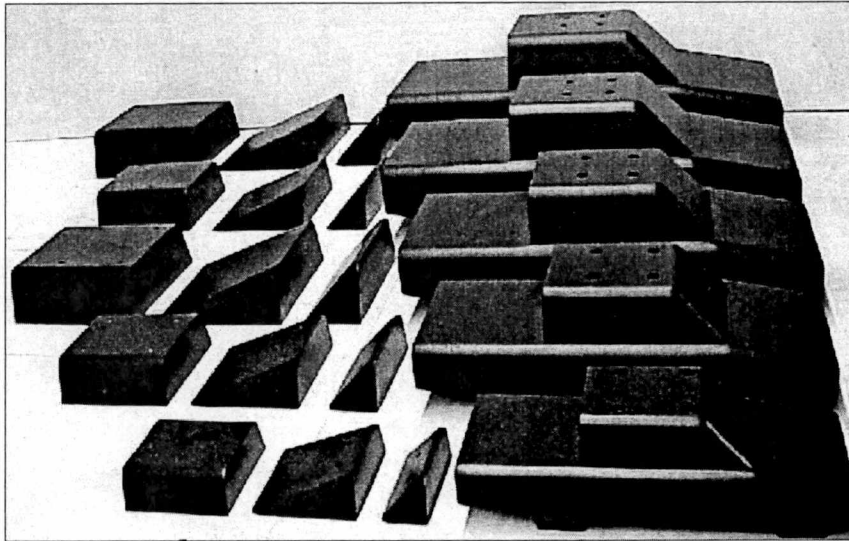
Blockage *, %	11	15	20	25
Model Scale **	0.096	0.112	0.129	0.144
Width (1)	6.128	7.157	8.264	9.236
Half width (2)	3.064	3.578	4.132	4.618
Overall height (3)	4.974	5.810	6.709	7.499
Body height (4)	4.585	5.355	6.184	6.912
Clearance (5)	0.389	0.455	0.525	0.587
See ID (6)	2.660	3.107	3.588	4.010
See ID (7)	1.926	2.250	2.598	2.904
Length (8)	15.709	18.347	21.186	23.678
See ID (9)	3.991	4.661	5.382	6.015
See ID (10)	6.742	7.874	9.092	10.162
See ID (11)	4.999	5.838	6.742	7.535
See ID (12)	2.843	3.320	3.834	4.285
See ID (13)	2.018	2.357	2.722	3.042
See ID (18)	2.660	3.107	3.588	4.010
Edge radii (19)	0.504	0.589	0.680	0.760

Figure 6. MIRA Model geometry with tabulated dimensions (dimensions in inches).



Dimension	Expedition	Explorer
<b>W</b>	7.15	6.38
<b>y</b>	7.35	6.44
	6.08	5.31
	5.15	4.47
<b>R</b>	0.73	0.73
<b>Length</b>	18.60	17.34
<b>L1</b>	8.36	7.79
<b>HOL</b>	4.65	4.34

Figure 7. SUV Model geometry with tabulated dimensions (dimensions in inches).



**Figure 8. MIRA models shown with various modification blocks.**

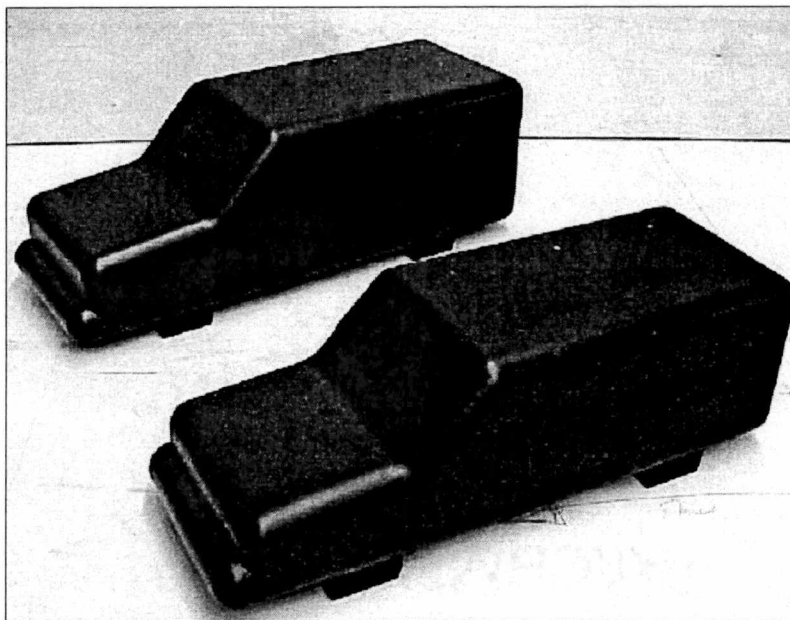


**Figure 9. The Small SUV and Large SUV (Before wheels were removed).**

A validation model was included in the study to confirm the effectiveness of the derived correlation. This model, a MIRA 15% blockage fastback with a rear spoiler, was tested in both the open jet test section and adaptive wall test section, but the measured data were not used in developing the correction equations. This permitted an independent “check” on the correction equations. An image of the validation model is shown in Figure 10.

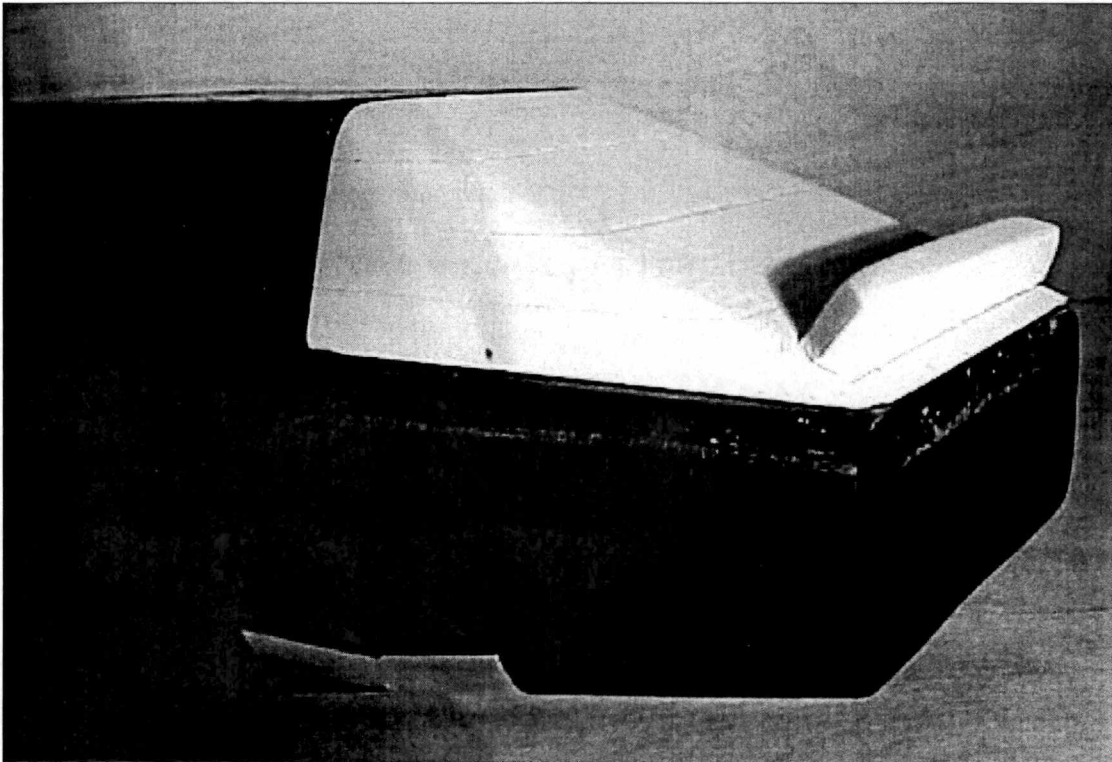


**Figure 10. Back end of validation model.**



Reynolds number, which was based on model length, was held constant for all experiments. For a given wind speed, the minimum vehicle length from the ensemble of models defines the upper bound for Reynolds number. The maximum achievable wind speed in the wind tunnel is the other constraint. The minimum Reynolds number that could be obtained in the test configuration was  $1.6 \times 10^6$  (up from  $1 \times 10^6$  in the first study, where a shorter model was included). This 60% increase moves the typical model drag coefficient into a more stable, flat region of the  $C_D$  versus  $Re$  curve plotted in Figure 11. This  $C_D$  versus  $Re$  trend for the MIRA Fastback shape is consistent with data published in the SAE document on open jet interference, J2071. The basic motivation for holding  $Re$  constant in the current study was to eliminate any Reynolds number effects in the data set, thereby isolating aerodynamic "interference" effects.

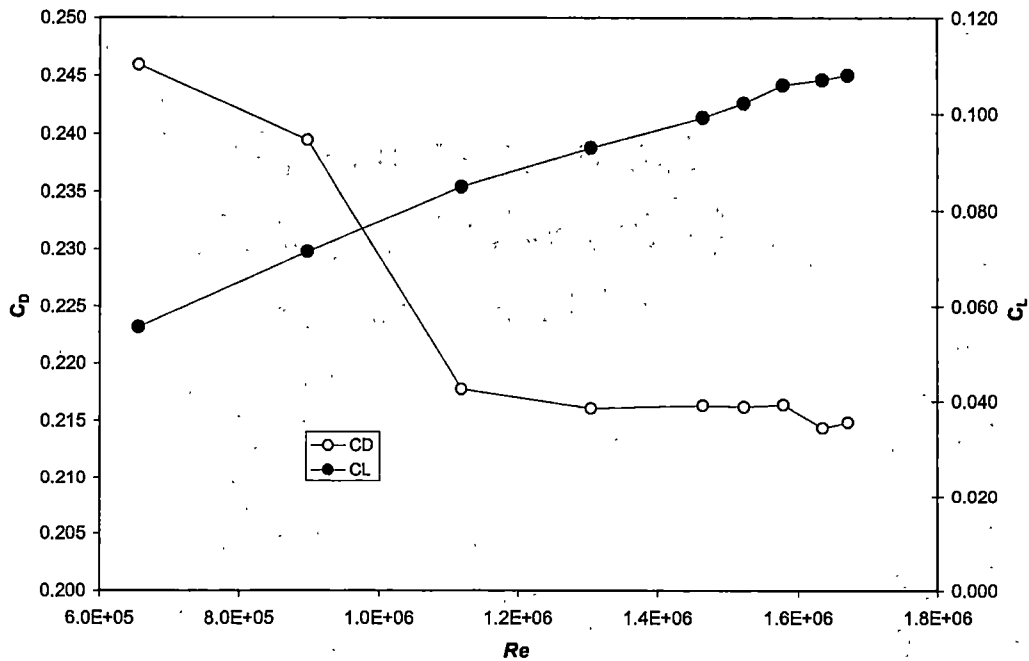


Figure 11.  $C_D$  and  $C_L$  as a function of Reynolds number (Fastback model).

All four "half-wheels" were removed from the underside of each model. Because the boundary layer thickness was on the order of the ground-to-model underbody clearance, the wheels would be partially, if not wholly, submersed in the boundary layer, causing complicated acceleration effects beneath and around them. While a smooth underbody has been shown to affect drag results, the exact effect on lift was unknown (Ahmadi et al., 1996). Removing the wheels simplifies the underbody effects of the models by removing the wheel/boundary layer interaction, which would vary with model scale (varying wheel size and varying proximity of the wheels to the floor).

Ground clearance (the distance from the test section floor to the vehicle underbody) was held constant at 1.07 inches for all tests, excluding those tests expressly intended to study boundary layer effects. That height was selected for two reasons: first, it is slightly greater than the boundary layer thickness; and secondly, it matches the ground clearance of several models in Hoffman's earlier study (Hoffman et al., 2001). Holding the ground clearance constant (as opposed to raising or lowering a model based on its size) was intended to maintain constant underbody effects for all models.

### **Open Jet Wind Tunnel Configuration**

Figure 12 shows a diagram of the setup, including the pressure tap location used to determine the differential static pressure across the contraction section. The downstream pressure tap is located 65 inches upstream of the balance center, sufficient to avoid upstream interference in the current test section configuration (Hoffman et al., 2001). Figure 13 shows a detailed drawing of the test section. An image of the open jet setup is shown in Figure 14.

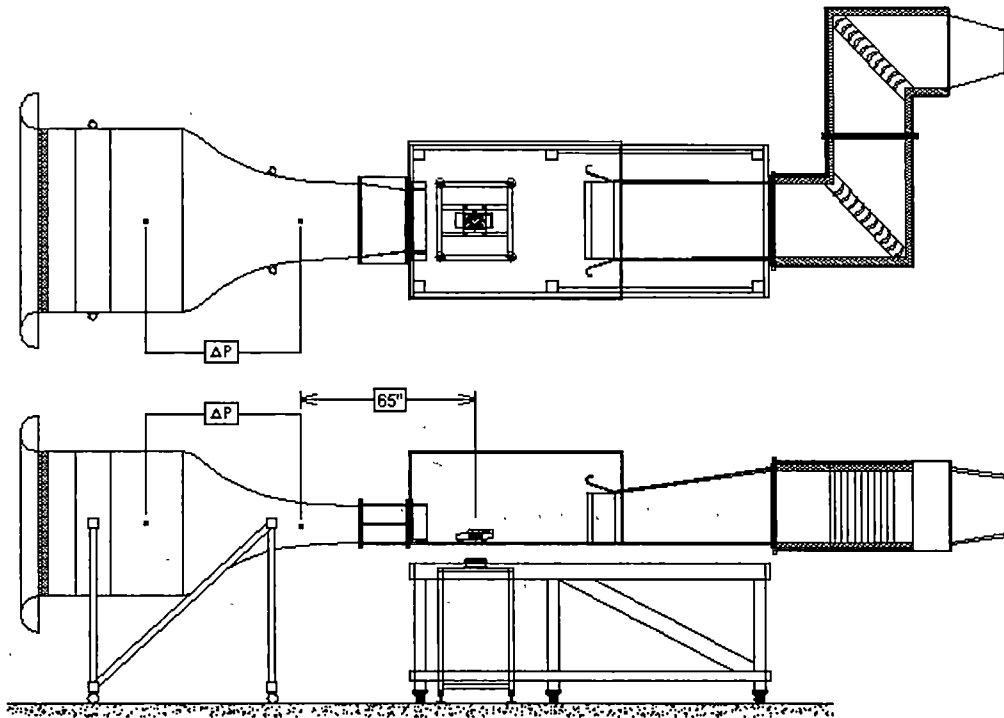


Figure 12. Overall open jet wind tunnel configuration.

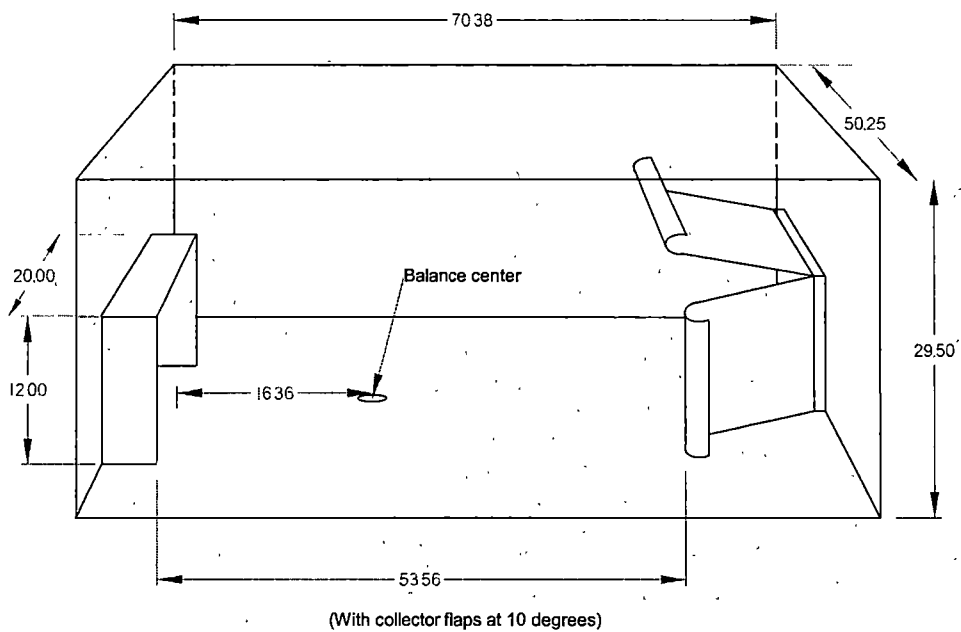
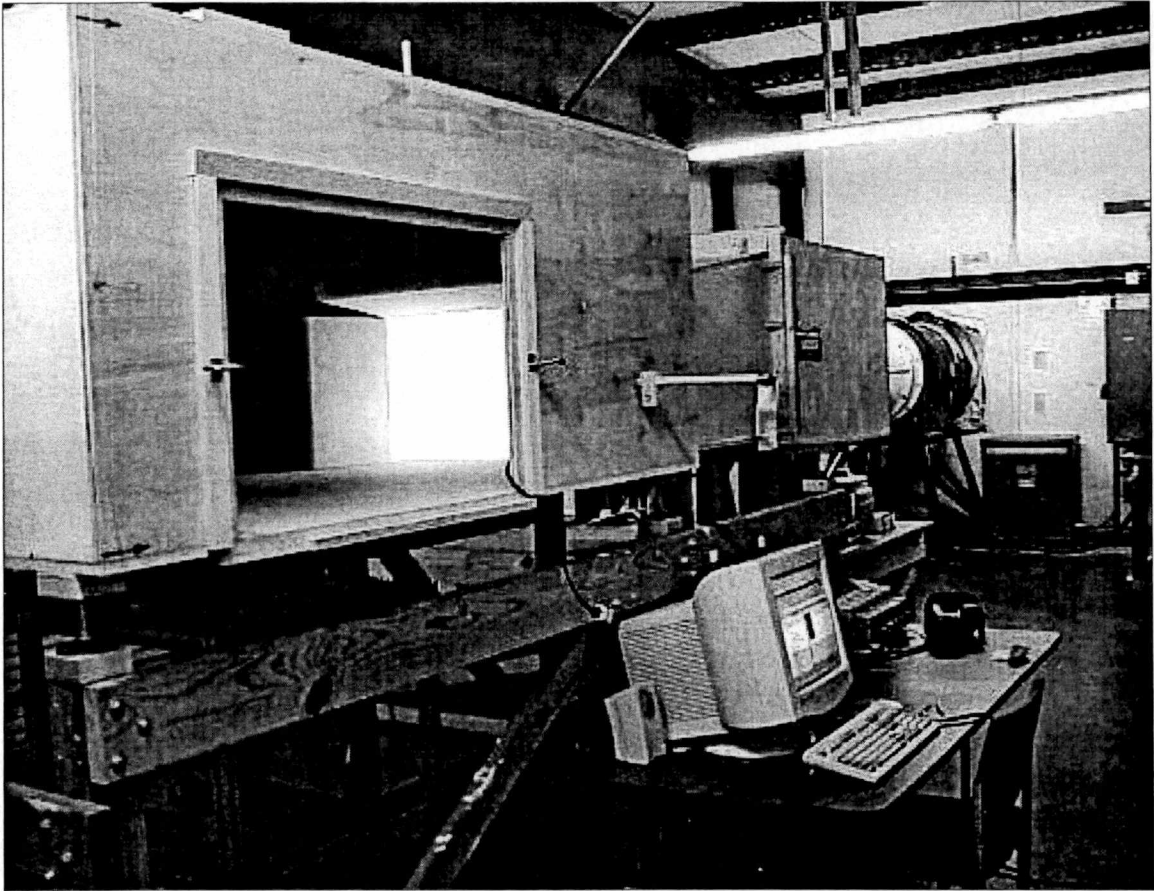


Figure 13. Open jet wind tunnel (Dimensions in inches)



**Figure 14. Image of scale model setup showing open jet plenum with inset collector flaps.**

An open circuit arrangement was used, extending from the contraction to the test section, then downstream through a high-speed diffuser to two acoustically treated corners that redirected the flow towards the fan. This configuration replicates the boundary influences around the model in the test section, and creates the gross effects of the corners and contraction. The acoustic treatment in the corners had the added benefit of suppressing fan noise propagation into the test section that, if high enough, could possibly have influenced the aerodynamic coefficient measurements.

Wind tunnel pressures were measured using a Scanivalve<sup>®</sup> transducer, signal conditioner and switching unit. The pressure measurement equipment was located next to the test section. Each pressure port was measured sequentially, with a sample time of 5 seconds for each port. The data were then time averaged and the switching unit stepped to the next port. The time required to initialize the data acquisition process allowed the pressure to stabilize. Both this time-averaging procedure and the employed lengths of pressure tubing acted as low-pass filters on the measured pressures, making it simple to acquire the desired average pressures. All data were acquired for 5 seconds at 100 Hz using a 200 MHz PC and National Instruments PCI-6031E data acquisition card.

### **Adaptive Wall Wind Tunnel Configuration**

A photograph of the adaptive wall wind tunnel setup is presented in Figure 15. The circuit utilized the contraction section from the open jet configuration, the adaptive wall test section, and a diffuser section that lead to the fan. The test section consists of twelve 96-inch long flexible panels arranged with three slats on each wall, and six slats on the ceiling. Wiper blades form airtight seals between each slat, sealing off the test section from ambient air. Manually adjustable jacks that are located at axial locations along the test section control the wall shape. Seventeen such jacks are located on each of the twelve slats for adjustment of wall shape. The adaptive wall test section is 12 inches high and 24 inches wide at the inlet. A diagram of the adaptive wall test section is shown in Figure 16.

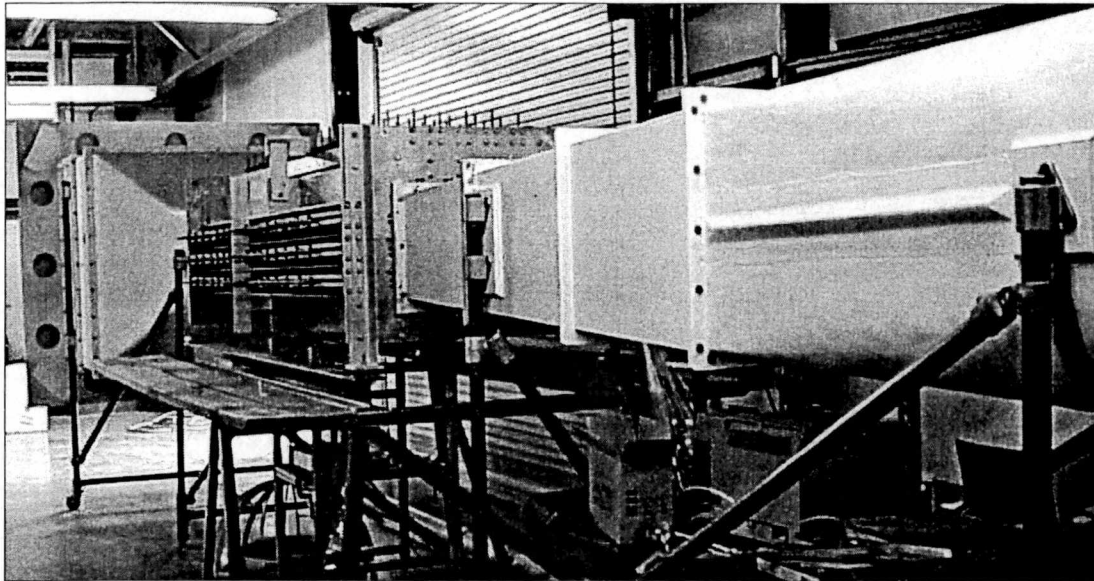


Figure 15. Photograph of adaptive wall test section setup.

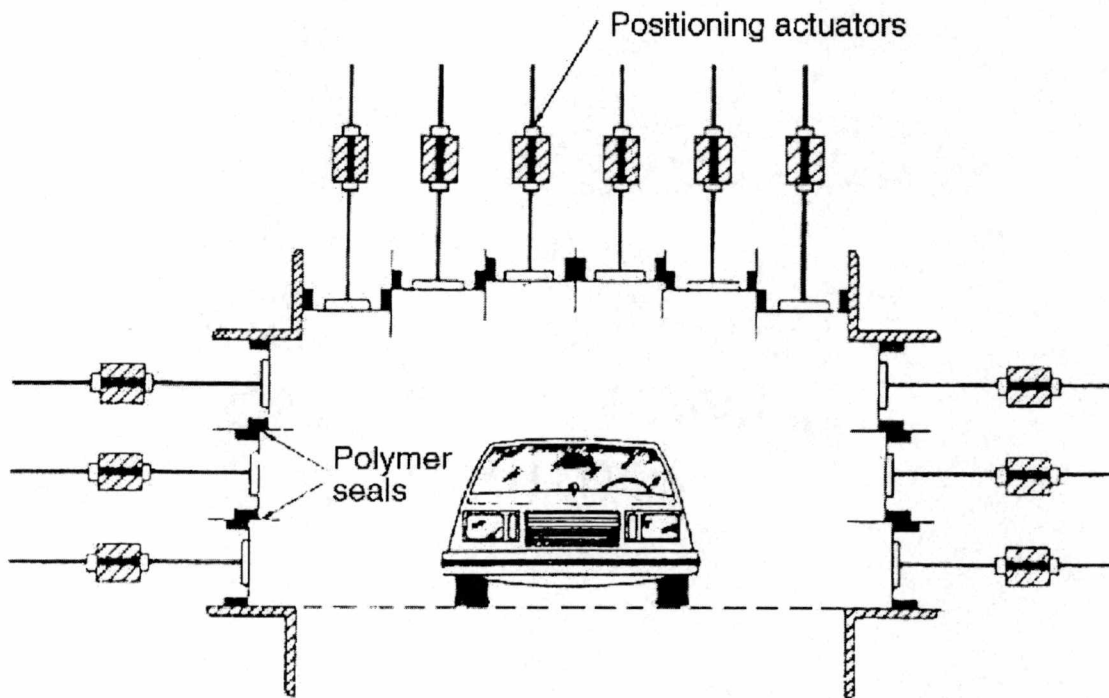


Figure 16. Diagram of adaptive wall test section.

Source: Hucho, Wolf-Heinrich, "Aerodynamics of Road Vehicles" 4<sup>th</sup> Edition, Society of Automotive Engineers, Inc., Warrendale, PA, 1998.

### Dynamic pressure measurement (Adaptive wall)

The adaptive wall tests used the differential pressure across the contraction section to indicate test section dynamic pressure. A calibration was performed that was similar to that carried out for the open jet testing. The dynamic pressure measured with a pitot-static tube inserted into the test section was plotted against the differential pressure between two sets of static pressure taps in the nozzle, each at a different axial location. This data is plotted in Figure 17. The relationship between the actual tunnel dynamic pressure and that measured by the nozzle static taps is:  $\Delta P_{\text{Nozzle}} = 0.583 \cdot \Delta P_{\text{Probe}}$ , where  $\Delta P_{\text{Nozzle}}$  is the pressure differential across the nozzle and  $\Delta P_{\text{Probe}}$  is the difference between the dynamic and static pressures measured with the pitot-static probe.

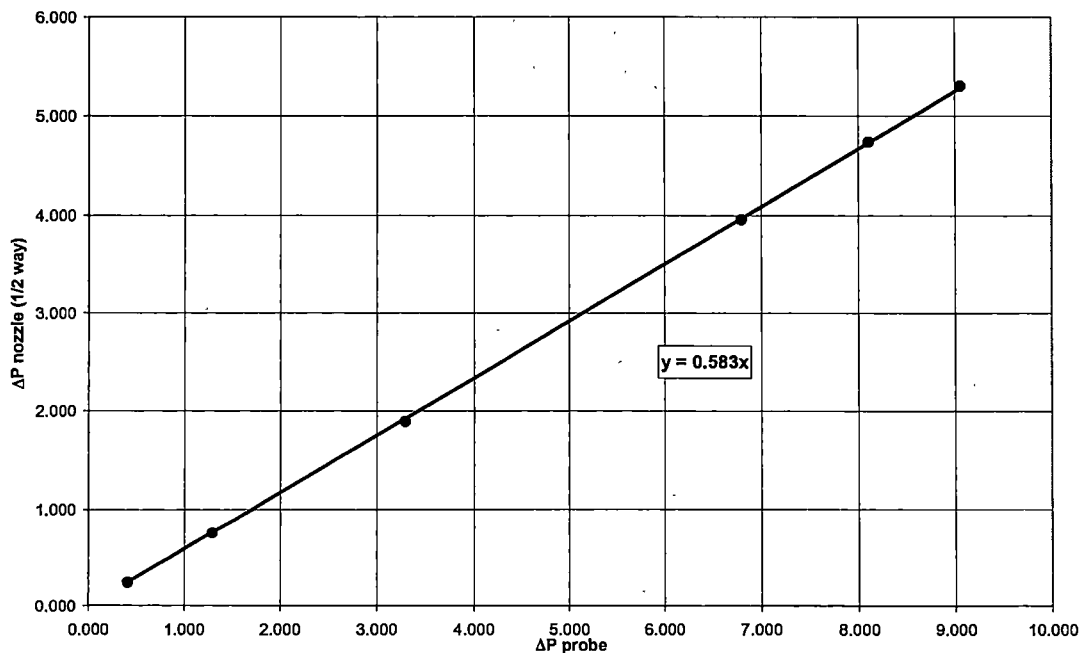


Figure 17. Adaptive wall dynamic pressure calibration.

Correct placement of pressure taps is critical for accurate dynamic pressure measurement using the nozzle method. Locating a tap too close to the model yields inaccurate static pressure readings due to the tap's proximity to model's upstream stagnation region. Conversely, distance is required between the upstream and downstream pressure taps so that the area change creates a pressure difference. Therefore, the distance used in Hoffman's study was adopted. This distance (47 inches upstream of the largest model) was shown to be out of the stagnation region while still providing sufficient area change to determine dynamic pressure (Hoffman et al., 2001). Adopting the square root of the frontal area as the characteristic length, this corresponds to approximately six length scales for the largest model. The calibration shown in Figure 17 was used to compute the actual dynamic pressure in the test section for all adaptive wall tests.

### **Adaptive Wall Measurements**

Reference aerodynamic coefficients were obtained with an adaptive wall test section. These values were considered the "correct" values when computing the correlation to interference-free measurements.

The adaptive wall test procedure is as follows. The models were centered in the spanwise direction, and located near the center of the test section axially. Static pressure distribution along each slat is measured, indicating the local flow velocity. The current position of the slats is also measured, indicating the local wall angle, and therefore the local flow angle. These inputs are used to predict a more streamlined wall shape using an algorithm developed by Sverdrup Technology for the adaptive wall test section (Whitfield et al., 1982). Adjusting the wall jacks generates the next wall shape



iteration. Wall static pressure and position measurements are acquired and the entire process repeated until the changes in wall position are less than 0.005 inches. Previous work has shown that fully converged adaptive wall measurements yield results free of any wall interference effects (Arnette et al., 2001; Goenka et al., 1990; Whitfield et al., 1982). A more detailed explanation of the theoretical background and principle of operation for the adaptive wall test section can be found in these references.

The test section wall shape was adjusted using the manual jack screws until additional iterations resulted in negligible changes to the aerodynamic coefficient results (defined as a change in drag coefficient of less than 1%). At this point, the final “interference-free” reference coefficients were measured.

**Force Balance**

A six-component balance, manufactured by Modern Machine and Tool, was employed to measure aerodynamic model forces and moments. The balance was mounted internal to the models in a cavity—eliminating the need to place a pressure seal between the test section plenum and the ambient air. The balance measurement characteristics are shown in Table 1, which shows that the balance does not measure lift forces as accurately as the other components. This is because it is designed for sidewall mounting in a wind tunnel—a typical configuration for testing 2-D wing models.

**Table 1. Measurement characteristics of employed force balance.**

Component	Lift	Drag	Pitch Moment	Roll Moment	Yaw Moment	Side Force
Limit (lb or in*lbs)	10	10	75	168	168	25
2-σ error (%)	4.3	0.22	0.21	0.09	0.03	0.06

In those tests, the component normal to the balance surface (lift force in the current mounting scheme) corresponds to side force on a wing model, which is not measured for 2-D airfoil tests. Previous tests confirmed that shifts in the data due to thermal drift and preloading are on the order of the lift forces, making the employed balance unsuitable for reliable lift measurements. Therefore, another lift measurement technique was needed that could provide better accuracy without significantly altering the previously used balance configuration.

Model lift was measured using three small load cells fastened to the bottom surface of the balance, as shown in Figure 18. The load cells mounted to a plate that was fastened to a rotation stage with a 3/8-inch diameter rod, which passed through the test section floor. The entire assembly (including the model) could be rotated 360 degrees allowing any yaw angle to be set. The entire balance/load cell assembly fit inside each model in a cavity designed for mounting the balance. This balance/load cell assembly is shown mounted inside a typical model in Figure 19 using a double-exposure photograph.

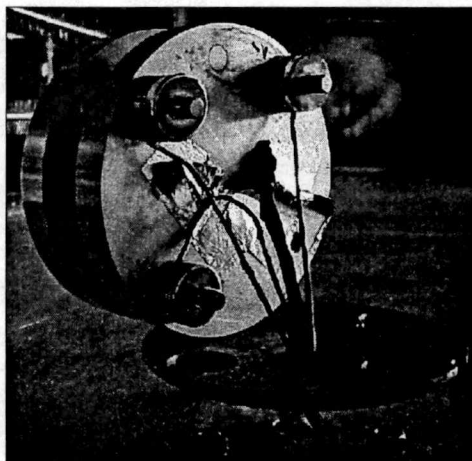


**Figure 18. Image of load cell arrangement (balance is tilted on its side).**

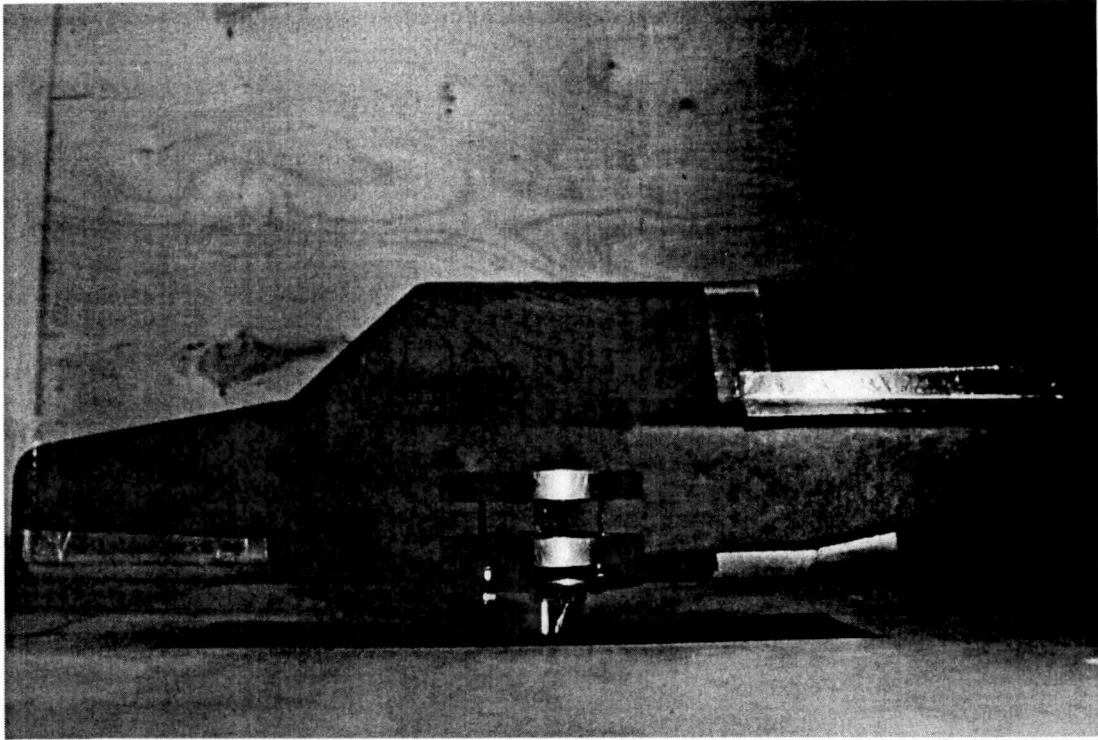


**Figure 19. Double-exposure photograph showing how balance mounts inside model.**

The load cells offered a good compromise between size and accuracy. They had to be small enough to fit into the existing models without significantly altering the configuration, and needed to provide enough accuracy to resolve the expected loads. The load cells selected have a 0.25-inch height (not including threaded ends) and are accurate to 1% of full-scale (*Omega* part number LC201-25). Because all lift force is transmitted through the load cells, the total lift force is determined by summing the forces in the vertical direction, as measured by the calibrated load cell outputs. The load cells were individually calibrated before being attached to the force balance. The load cell output is linear, as can be seen in a typical calibration curve (Figure 20).

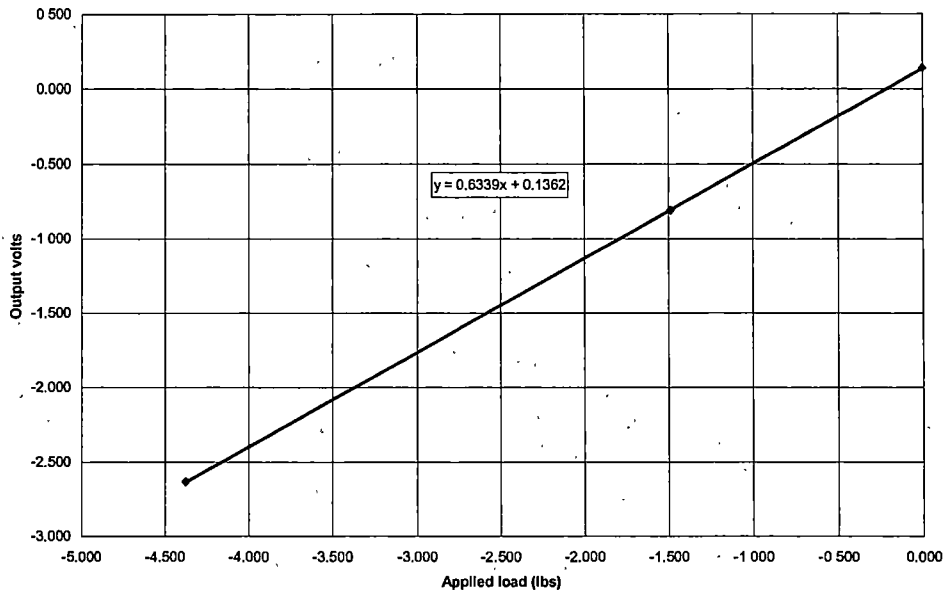


Figure 20. Typical load cell calibration curve.

### **Methods of Open Jet Dynamic Pressure Measurement**

In the open jet test section, dynamic pressure was measured using both the nozzle and plenum methods. The nozzle method measures the differential static pressure between two points in the contraction section, and relates that pressure to test section velocity using standard incompressible flow calculations. Considerable attention must be paid to this measurement because of its direct effect on aerodynamic coefficient results. Since dynamic pressure is the normalization parameter in aerodynamic coefficient calculations, an error in dynamic pressure measurement translates directly to an error in the aerodynamic coefficient. For example, a 1% error in dynamic pressure translates to a 1% error in the aerodynamic coefficient result.

Upstream model influence contributes to dynamic pressure measurement errors using the nozzle method. This upstream interference was quantified in Hoffman's open jet

study. The results of that experiment showed that the pressure tap locations selected in the nozzle were sufficiently upstream of the stagnation region in front of the model. Therefore, these pressure measurement locations were maintained for the current study.

Dynamic pressure was also obtained using the plenum method. In this technique, differential static pressure is measured between the stilling chamber and a point in the plenum, which is then related to test section dynamic pressure. Several static pressure taps were placed in the plenum to permit data analysis using the plenum method of dynamic pressure measurement. The locations of these taps are specified in Figure 21. The nozzle height in the subscale model (12 inches) is shown in the figure for purposes of scaling the tap locations to the full-scale facility.

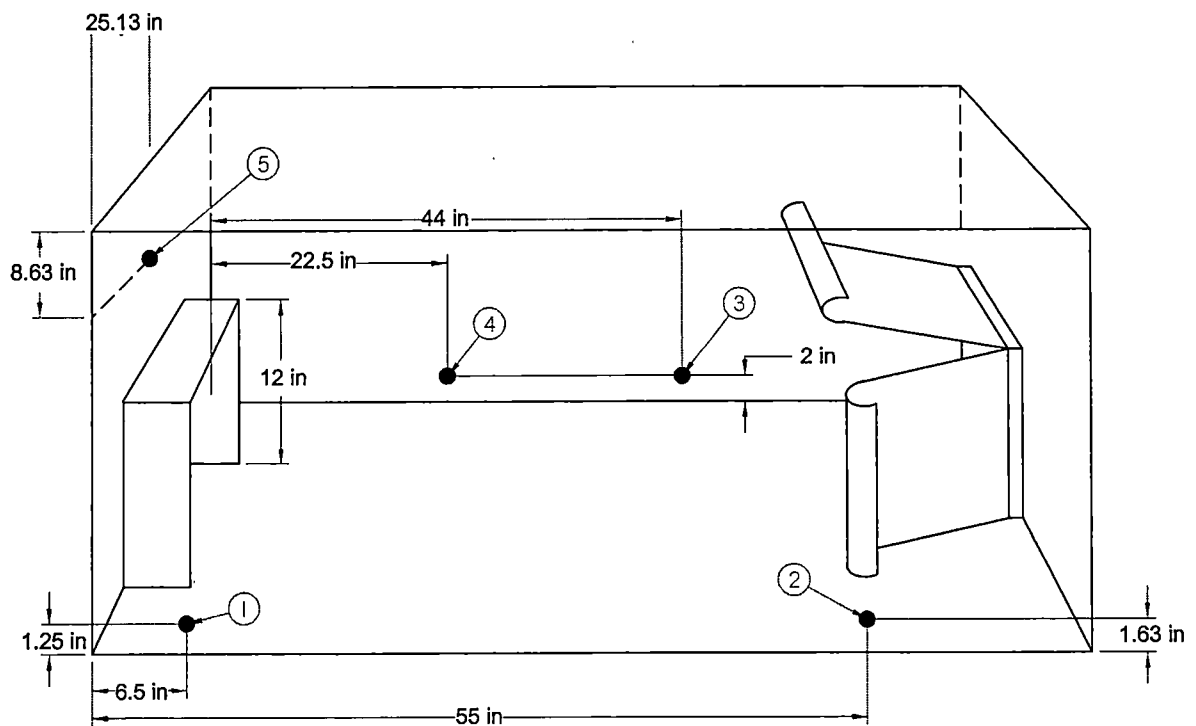


Figure 21. Diagram of plenum pressure taps placement in open jet model.

Plenum taps located in the full-scale facility were replicated in the subscale model; the other taps were included to define the sensitivity of tap location when using the plenum method. Previous work has shown that the presence of a model in the test section may alter the dynamic pressure reading—suggesting that the plenum method may be more sensitive to model placement and geometry than the nozzle method (Kuenstner, 1992). Neither the nozzle method nor the plenum method has emerged in the wind tunnel testing community as the primary way to measure dynamic pressure.

The relationship between the differential pressures at the tap locations and the test section dynamic pressure was determined over a range of velocities in the empty test section. The results of this calibration are shown in Figure 22.

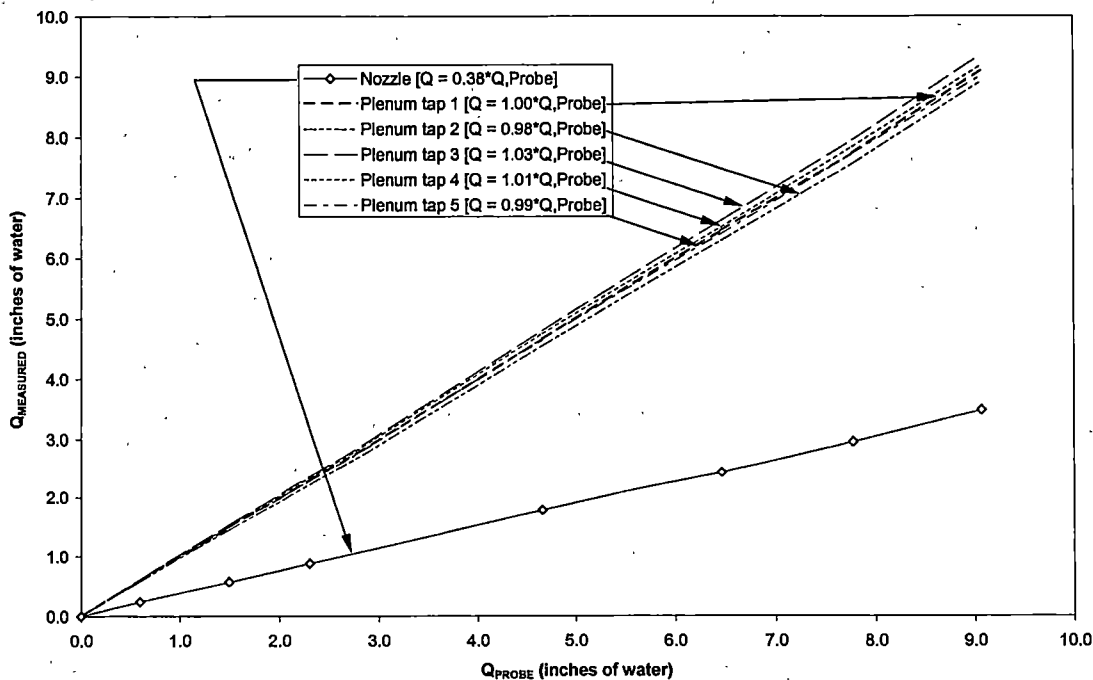


Figure 22. Open jet dynamic pressure calibration.

The data show that dynamic pressure measured using the plenum method is relatively insensitive to tap location for empty test section measurements. This can be seen by looking at the slopes of the calibration lines shown in Figure 22. The slopes do not vary significantly for the taps located in the plenum, (less than 3 percent at most). This shows that for empty test section dynamic pressure measurements, the dynamic pressure measurement is virtually independent of plenum tap location. However, for dynamic pressure measurements made with a model installed, this is not true. This is demonstrated in the results presented below.

Comparing the  $C_D$  as a function of blockage for the nozzle method and the plenum method shows an interesting result. For a given model, the range of  $(C_D - C_{D,0})/C_{D,0}$  using the nozzle method is typically larger than the plenum method in the current data sets, where  $C_{D,0}$  is the reference drag coefficient measured in the adaptive wall. In the case of the pickup (Figure 23), the  $(C_D - C_{D,0})/C_{D,0}$  range is near zero, but the overall "error" is consistently less than zero. This conclusion is consistent with the findings of Kuenstner et al., which showed that plenum-referenced dynamic pressure data generally yields lower drag coefficients. Data for the MIRA models used in the study (pickup, fastback, and squareback) are shown in Figure 23 through Figure 25, respectively.

### **Ground Effects**

Floor boundary layers have been shown to influence both drag and lift data in wind tunnel measurements. Fundamentally, the viscous boundary layer present beneath the car in the wind tunnel is not present under the car on the road. This affects the wind tunnel's ability to provide a replication of the on-road environment.

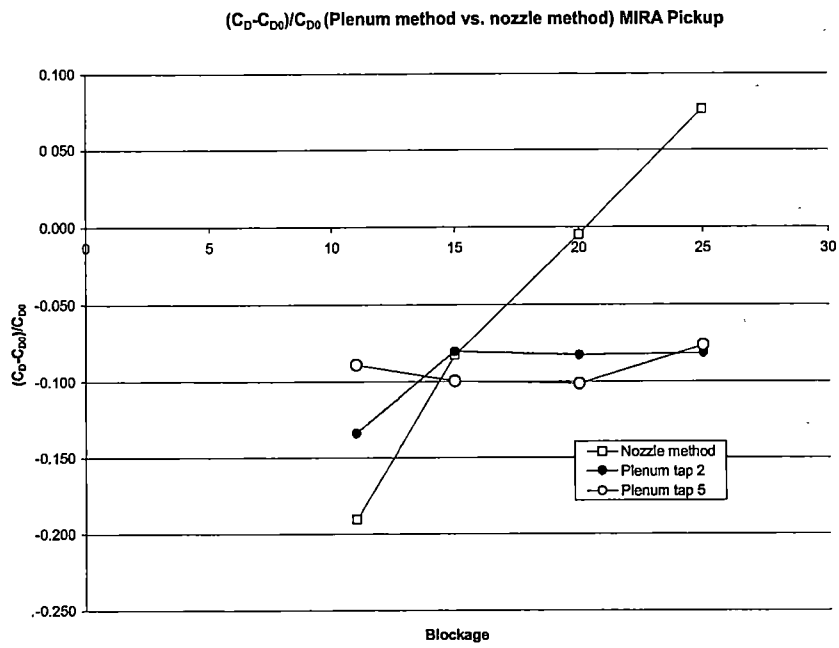


Figure 23.  $(C_D - C_{D,0})/C_{D,0}$  for Q measurement methods (MIRA Pickup).

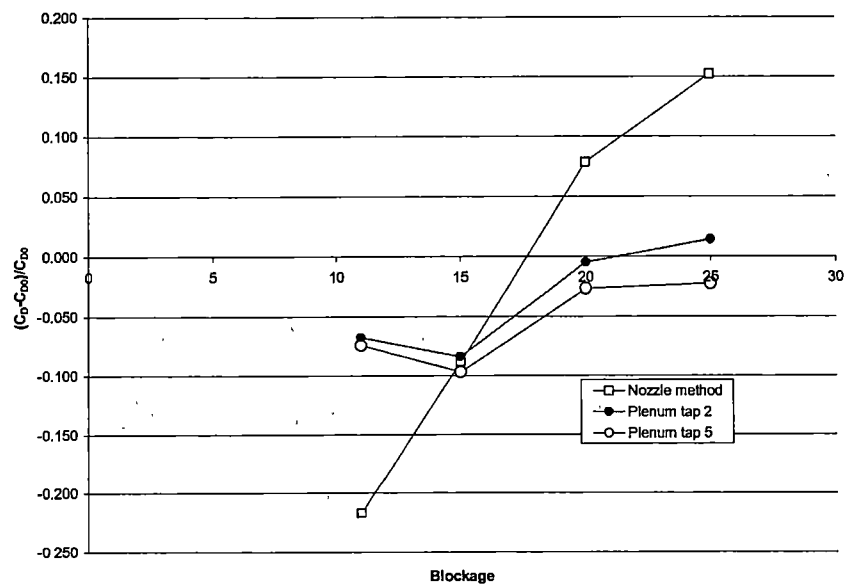


Figure 24.  $(C_D - C_{D,0})/C_{D,0}$  for Q measurement methods (MIRA Fastback).



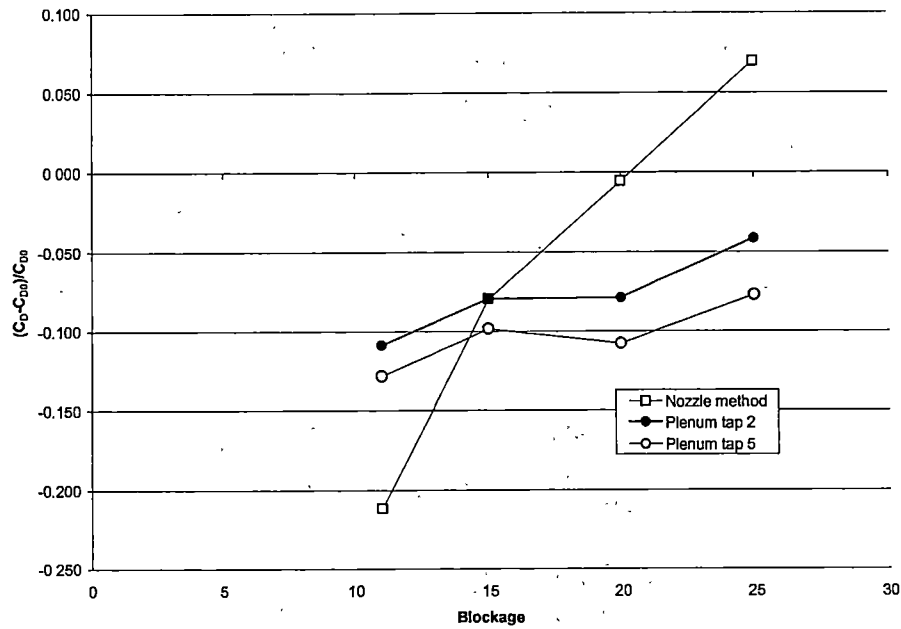


Figure 25.  $(C_D - C_{D,0})/C_{D,0}$  for Q measurement methods (MIRA Squareback).

In the current study, however, open jet effects are quantified by comparing between two test sections with fixed ground planes. By matching  $Re$  and model ground clearance between the open jet and adaptive wall tests, the boundary layer effects are the same in the open jet and adaptive wall test sections. This isolates the open jet interference effects without requiring boundary layer corrections. However, it should be noted that boundary layer flow still pollutes both open jet and adaptive wall data sets.

A boundary layer correction was investigated as a possible approach to adjust the data for boundary layer influence. However, when the adjustment was applied to the adaptive wall data, the data changed from being independent of blockage (which is the expected trend for adaptive wall measurements) to varying significantly with blockage.

This was a strong indication that the boundary layer adjustment would probably inject more harm than good into the study.

*No boundary layer corrections were applied to the data* because (i) the correction method does not have a solid physical basis, (ii) any 'reasonable' boundary layer correction was found to cause the adaptive wall results to vary with model blockage, which should not occur, and (iii) equivalent ground-plane effects occur in both test sections (open jet and adaptive wall) and therefore do not invalidate any comparisons between the open jet and adaptive wall data.

Ground effects were quantified, however, to confirm that model height was sufficiently outside the floor boundary layer. Aerodynamic forces were measured on the MIRA 15 fastback in the open jet test section at constant speed. These forces were measured for a range of ground clearances that spanned the boundary layer thickness. The drag and lift coefficients at various ground clearances are shown in Figure 26 and Figure 27, respectively.

The abrupt change occurring near the middle of each plot corresponds to the boundary layer thickness, which was approximately 1 inch for the current tests. Examination of the plots shows that although the drag coefficient is more stable outside the boundary layer, the lift coefficient's behavior is quite different. It approaches the boundary layer thickness differently above and below, with the strongest downforce (smallest lift coefficient) occurring at the boundary layer height. Therefore, a vehicle placed at the boundary layer height is precariously positioned at the edge of two steep gradients—making it extremely sensitive to changes in ground clearance.

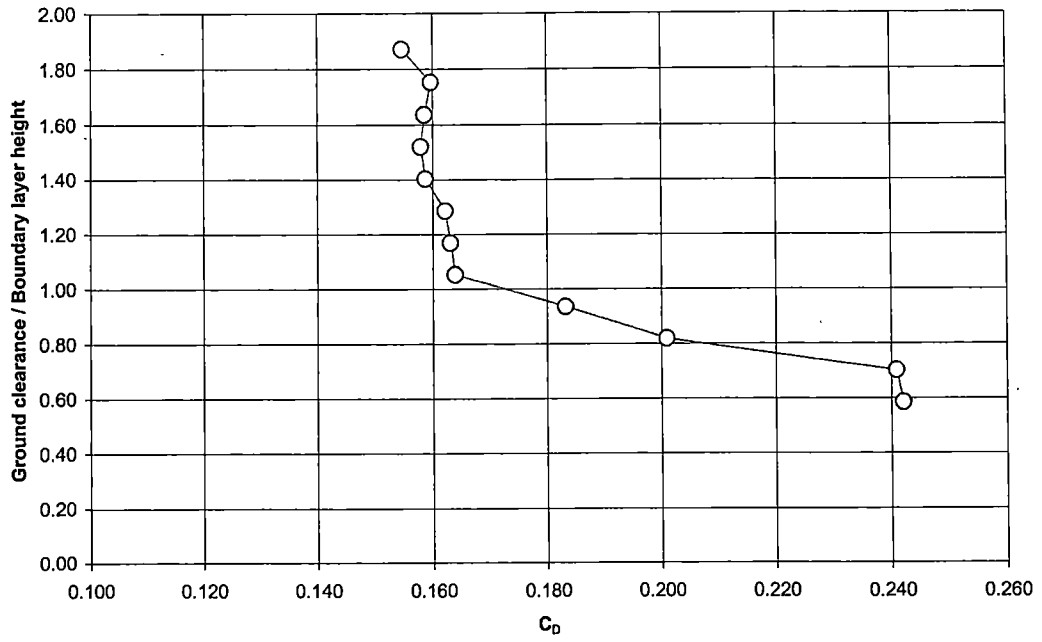


Figure 26.  $C_D$  as a function of ground clearance.

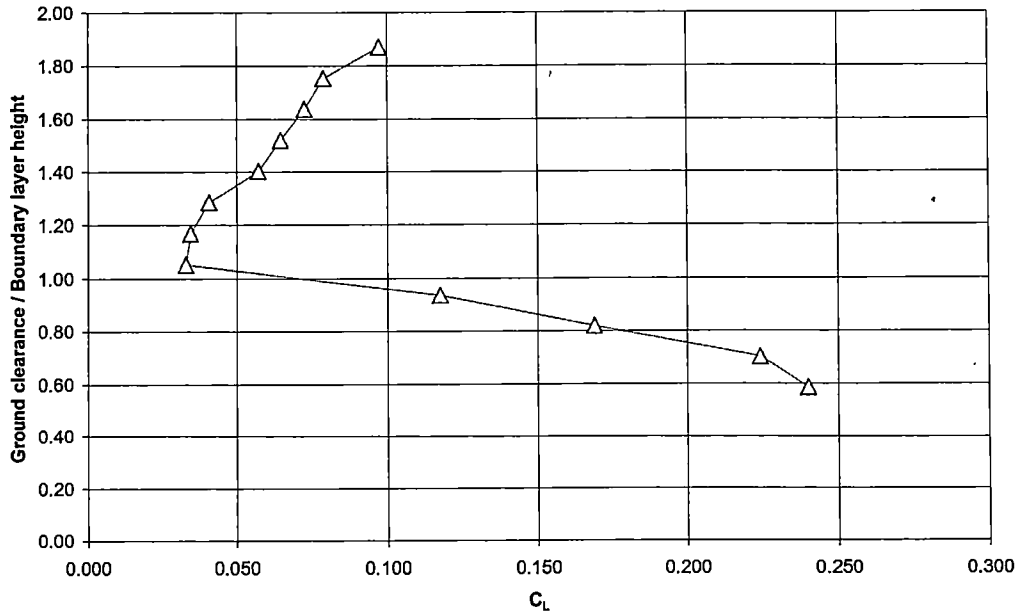


Figure 27.  $C_L$  as a function of ground clearance.

This type of experiment was also performed at the University of Maryland Wind Glenn L. Martin Wind Tunnel. The boundary layer thickness is approximately equal at that facility, and therefore the ground effects are similar, as well. Drag coefficient for a MIRA 15 fastback model was determined over a range of ground clearances, yielding the results shown in Figure 28. These data from the current study agree well with trends in the University of Maryland data. Both of these tests were performed on the MIRA 15 fastback; however, the wheels were removed in the current tests. Even with the slight model geometry variation (the wheels were still attached to the vehicle body in the UMD tests), the trends are strikingly similar. This suggests that the lift measurement scheme employed in the current study yields lift data that is accurate enough to extract meaningful trends.

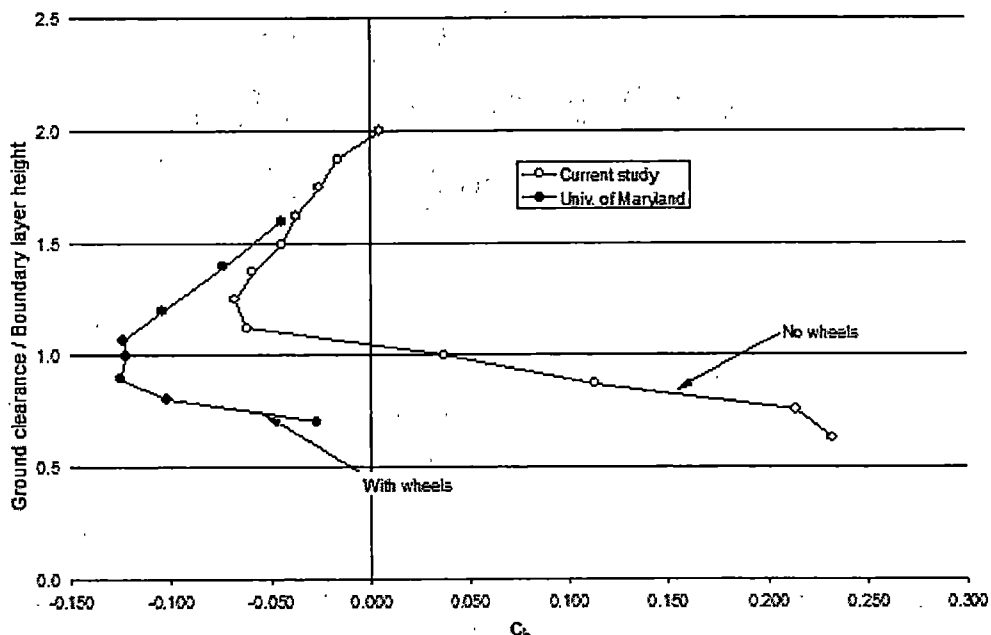


Figure 28. Comparison of  $C_L$  dependence on ground clearance (MIRA 15 fastback).

## Estimate of Experimental Error

An estimate of measurement uncertainty has been performed for a typical drag coefficient. Uncertainty is typically expressed in counts, which is defined to be one thousandths of a coefficient ( $C_D$  or  $C_L=0.001$ ). The results of this sample calculation are shown in Figure 29. For a  $C_D$  of 0.32 (typical for a squareback model), this calculation yields an uncertainty of  $\delta_{CD} = 0.003$ , or 3 drag counts. For reference, one-tenth of one count— $C_D$  or  $C_L=0.0001$ —is typically differentiated in full-scale automotive test facilities.

$$C_d = \frac{F}{\frac{1}{2} \rho V^2 \cdot A} = \frac{F}{q \cdot A}$$

$$C_d \pm \Delta C_d = \frac{F}{q \cdot A} \pm \frac{\partial C_d}{\partial F} \Delta F \pm \frac{\partial C_d}{\partial q} \Delta q \pm \frac{\partial C_d}{\partial A} \Delta A$$

$$\Delta A = \frac{\text{Perimeter}_{\min} \cdot 0.005''}{\text{Area}_{\min}} = 0.00043$$

$$\frac{\partial C_d}{\partial A} = \frac{\partial}{\partial A} (Fq^{-1}A^{-1}) = \frac{-F}{qA^2}$$

$$\Delta q = 0.0003$$

$$\frac{\partial C_d}{\partial q} = \frac{\partial}{\partial q} (Fq^{-1}A^{-1}) = \frac{-F}{q^2A}$$

$$\Delta F = 0.0435 \text{ lb}$$

$$\frac{\partial C_d}{\partial F} = \frac{\partial}{\partial F} (Fq^{-1}A^{-1}) = \frac{1}{qA}$$

$$C_d \pm \Delta C_d = 0.302 + \frac{1}{\left(14.843 \frac{\text{lb}}{\text{ft}^2}\right) \left(0.248 \text{ ft}^2\right)} (0.0022 \text{ lb}) + \frac{-4.932 \text{ lb}}{\left(14.843 \frac{\text{lb}}{\text{ft}^2}\right)^2 \left(0.248 \text{ ft}^2\right)} \left(0.0003 \frac{\text{lb}}{\text{ft}^2}\right) + \frac{-4.932 \text{ lb}}{\left(14.843 \frac{\text{lb}}{\text{ft}^2}\right) \left(0.248 \text{ ft}^2\right)^2} (0.0004)$$

$$= 0.302 + 0.000597 - 0.000027 - 0.002307$$

$$= \mathbf{0.302 \pm 0.0029}$$

Figure 29. Example uncertainty calculation on drag coefficient.

The measurement repeatability was estimated by repeating measurements for the same model. To capture all sources of uncertainty, the model was either removed or reoriented between consecutive measurements. For a given configuration, the model  $C_D$  repeated to within 1 drag count—much tighter than the 3 drag count uncertainty predicted by static calibration results.

Estimation of measurement uncertainty has also been performed for lift data. The load cell measurement uncertainty (as reported by the manufacturer) is 1% of full-scale, which includes linearity, hysteresis, and repeatability. However, because the three load cells are arranged in series with the balance, the total measurement uncertainty for lift will be larger than this specified value. If the total uncertainty in the lift measurement is assumed to be the square root of the sum of the squares, then the uncertainty associated with each measured load can be added, as illustrated in Equation 2.

$$\eta_{Total} = \sqrt{(\eta_{Load\ cell\ 1}^2 + \eta_{Load\ cell\ 2}^2 + \eta_{Load\ cell\ 3}^2)}$$

**Equation 2**

The load cells employed have a maximum load measuring capability of 25 pounds. If the above estimation of total uncertainty is adopted, then the total uncertainty for lift measurements is 0.43 lbs. This translates into an estimated 30 to 50 lift counts ( $C_L=0.030$  to  $0.050$ ) for the employed models. This amount of resolution permits trends to be seen over large spans in downforce where the measured forces are much greater than the measurement uncertainty. For lift data that hover near zero  $C_L$ , trends are harder to recognize because the actual measurements are on the same order as the uncertainty.

## Chapter 5

### Presentation of Experimental Results

For clarity, the model data are presented in two separate categories: MIRA models (including the validation model) and Sport Utility Vehicles. The nozzle method of dynamic pressure measurement was used to compute the aerodynamic coefficients. Also, recall that the model tests performed at the University of Maryland employed the models before the half-wheels were removed. The half-wheels were removed for the current study to avoid their influence on the lift results due to being partially submerged in the boundary layer. Therefore, a slight offset in either  $C_D$  or  $C_L$  is to be expected due to the additional aerodynamic obstruction beneath the vehicles. Published work puts this offset at approximately 0.030 for  $C_D$ . There are no known published works relating lift change to the presence of half-wheels.

#### **Open Jet: MIRA Models**

The trend of increasing  $C_D$  with increasing blockage (for a given vehicle shape) is evident, and confirms Hoffman's earlier results (Hoffman, 2001). Figure 30 shows this trend for several vehicle shapes. A notable difference between Hoffman's previous open jet results and the current open jet results is the apparent interference at higher blockage tests. In Hoffman's previous open jet work, the open jet data converged toward the estimated interference-free measurement, but most  $C_D$  values were higher than the reference value. This is potentially attributable to differences in underbody simulation between the two studies, caused by removing the "half-wheels".

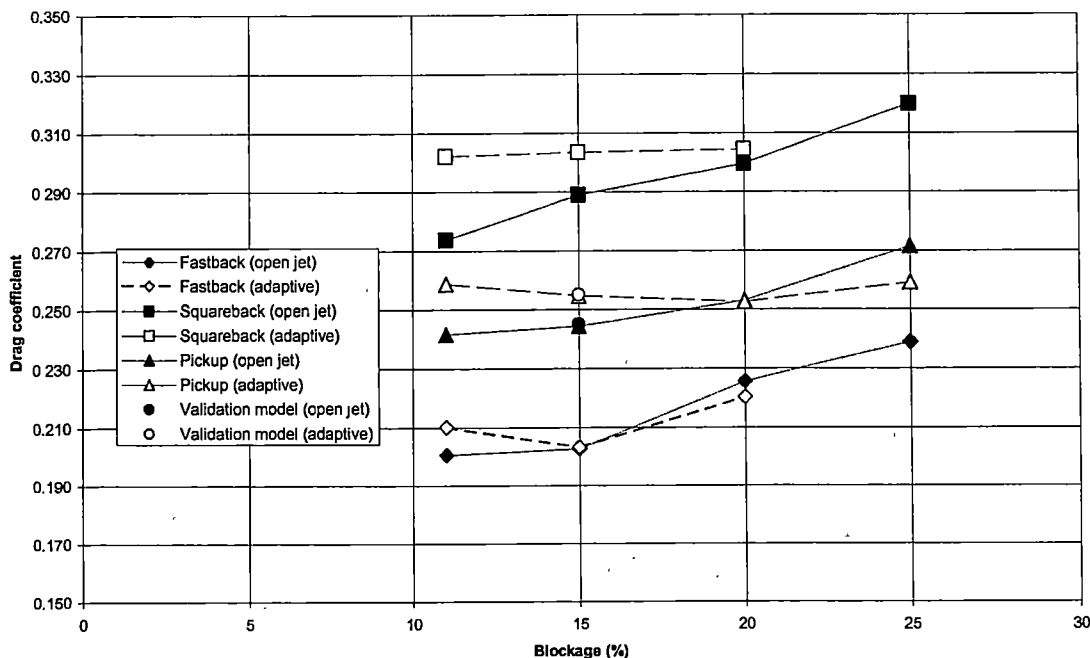


Figure 30.  $C_D$  values for the MIRA models (Open jet and adaptive wall).

Figure 30 shows that the open jet values intersect the adaptive wall data near 20% blockage for most models. This is likely attributable to the trend commonly seen in other open jet tests, in which the  $C_D$  measured in the open jet is below the reference number for medium blockage vehicles—typically in the 5% to 15% range (SAE Publication J2071).

Another observation is that  $C_D$  trend with increasing blockage is nearly flat for the adaptive wall tests. The pickup and squareback data are seen to yield virtually the same result regardless of blockage. This is a confirmation of the adaptive wall's ability to remove interference effects. The trend seen in the fastback (changing with blockage) is possibly due to Reynolds number effects. With only a small angle on the rear end of the vehicle relative to the flow direction, the flow separation point is not fixed, as it is in the



case of a squareback or pickup. This makes the separation point (and therefore the induced aerodynamic drag) very sensitive to slight variations in flow conditions. It is also possible that there are slight geometry variations between the different fastback models (imperfect tolerancing).

The University of Maryland measurements were taken to confirm the adaptive wall results. Some selected results are plotted in Figure 31 for comparison. Because the model blockage ratio was much larger in the adaptive wall test section than in the UMD tunnel, reference lines are shown for the adaptive wall data. This line is the average of all drag coefficients for a given model shape at all of the tested blockages in the adaptive wall. For example, the pickup  $C_D$  plotted is the average of the 11%, 15%, 20%, and 25% drag coefficients.

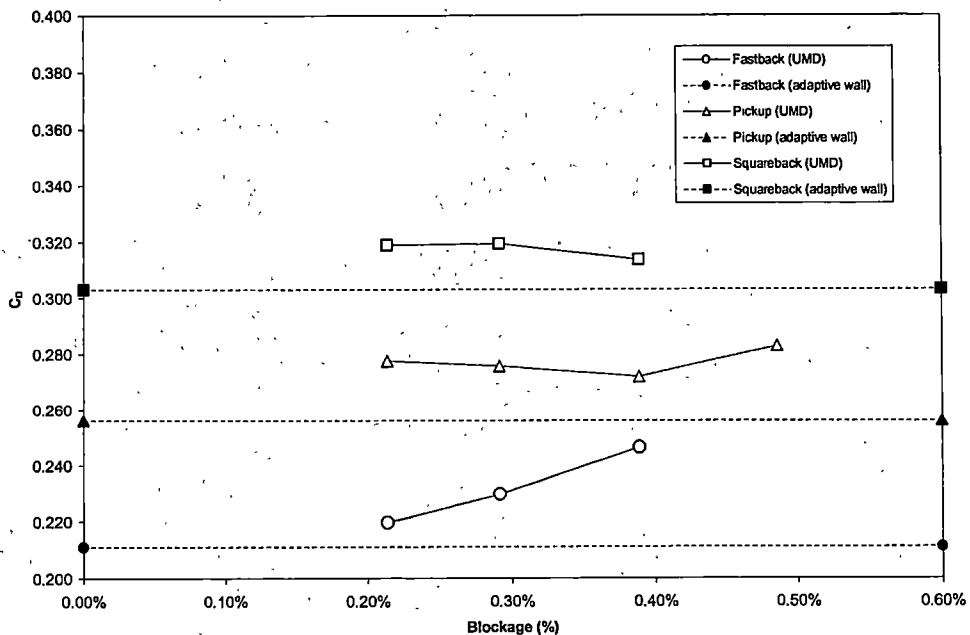


Figure 31.  $C_D$  values for the MIRA models (University of Maryland and adaptive wall).

The University of Maryland data compare well to the adaptive wall results. The extremely low model blockage in the UMD tunnel (less than 0.50% for all models) truly approaches the case of no boundary interference, with the exception of boundary layer effects—justifying the comparison to adaptive wall results. The slight offset between the UMD and adaptive wall data can be attributed at least in part to the presence of “half-wheels” during the UMD tests. The wheels were removed in the current tests, and likely account for the slight offset between the two data sets..

Figure 32 shows the open jet and adaptive wall lift coefficients for the models. Lift coefficient comparisons are difficult to make due to the limited amount of published data. However, several comments can be made regarding the trends in the data. For example, the squareback vehicles are shown to exhibit a large downforce (negative lift coefficient). While this seems contrary to intuition, it confirms data trends seen by Wallis and Williams in earlier tests for squarebacks with smooth underbodies (Wallis et al., 2001).

Also of note is that the addition of a rear spoiler to the MIRA 15 fastback (the validation model) had the net effect of increasing the downforce. This is consistent with published data for addition of a rear spoiler. While the lift coefficient is seen to decrease with increasing blockage in the open jet, this trend is also seen in the adaptive wall data. In fact, the open jet and adaptive wall results follow each other closely with blockage, suggesting that other effects dominate the test section effects on lift. This trend is seen for all of the MIRA models shown in Figure 32.

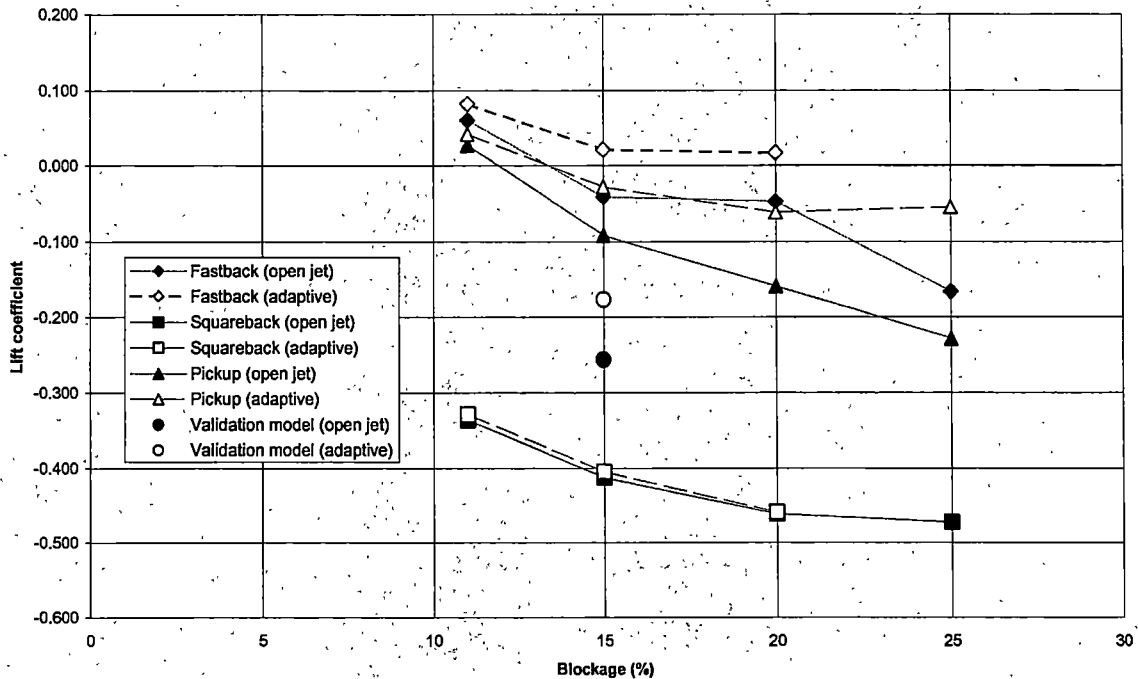


Figure 32.  $C_L$  values for the MIRA models (Open jet and adaptive wall).

Figure 33 illustrates the comparison between the lift coefficients acquired in the adaptive wall, and those acquired in the University of Maryland wind tunnel. Because the adaptive wall results should not change with vehicle size, they are presented as being constant with blockage—as indicated in the plot with the horizontal lines. The  $C_L$  values shown in Figure 33 show that trends between the UMD and current tests are consistent for lift. The slight downward trend in the Maryland data may be caused by the floor boundary layer effect. The overall comparison is quite good—even showing the offset caused by the removal of the “half-wheels” in the current tests. The largely flat profile of all plotted datasets indicate that the blockage effect minimal (due to the large cross-sectional area of the test section).

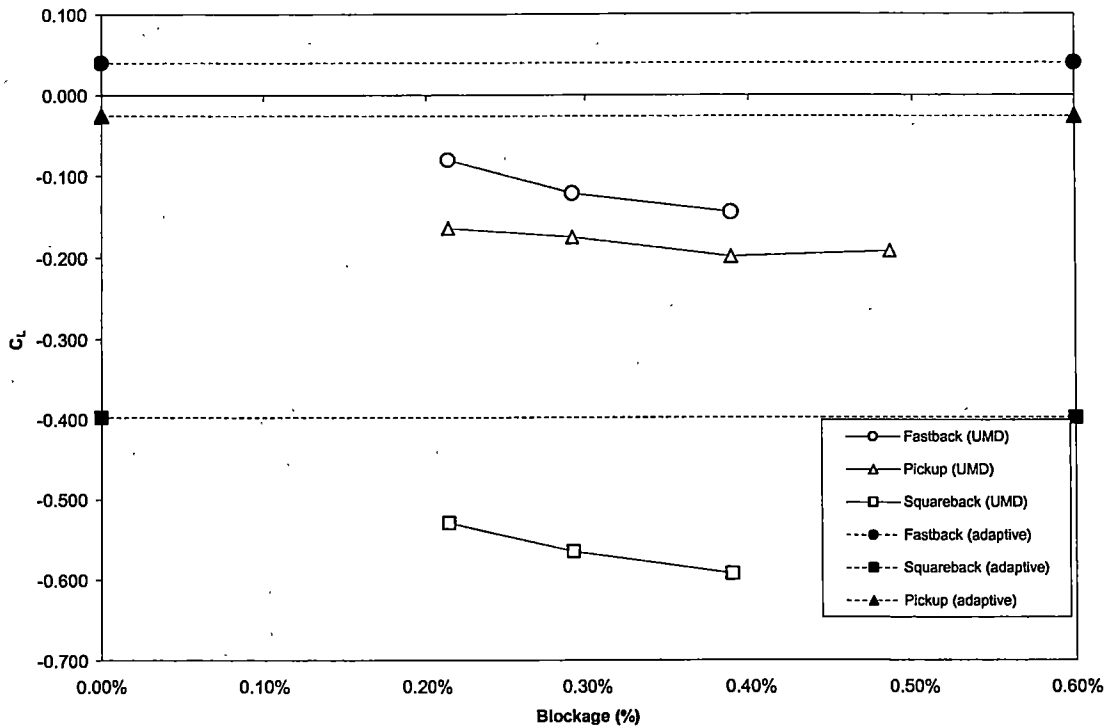


Figure 33.  $C_L$  values for the MIRA models (University of Maryland and adaptive wall).

### Open Jet: SUV Models

Care must be taken when examining the SUV model data trends. Contrary to the MIRA models, the SUV models are not simply larger scale versions of each other. While the width was maintained for each model size (small or large SUV), the height was changed. Therefore, trends relating model scale to measured aerodynamic coefficients cannot be extracted from the SUV data because model geometry was simultaneously changing.

Figure 34 shows drag coefficient values for the SUV models. These models exhibit behaviors also seen in the UMD data where there is a slight increase in the  $C_D$  of the middle SUV. A notable aspect of the plot is that all of the open jet SUV data are lower than the reference data obtained in the adaptive wall.

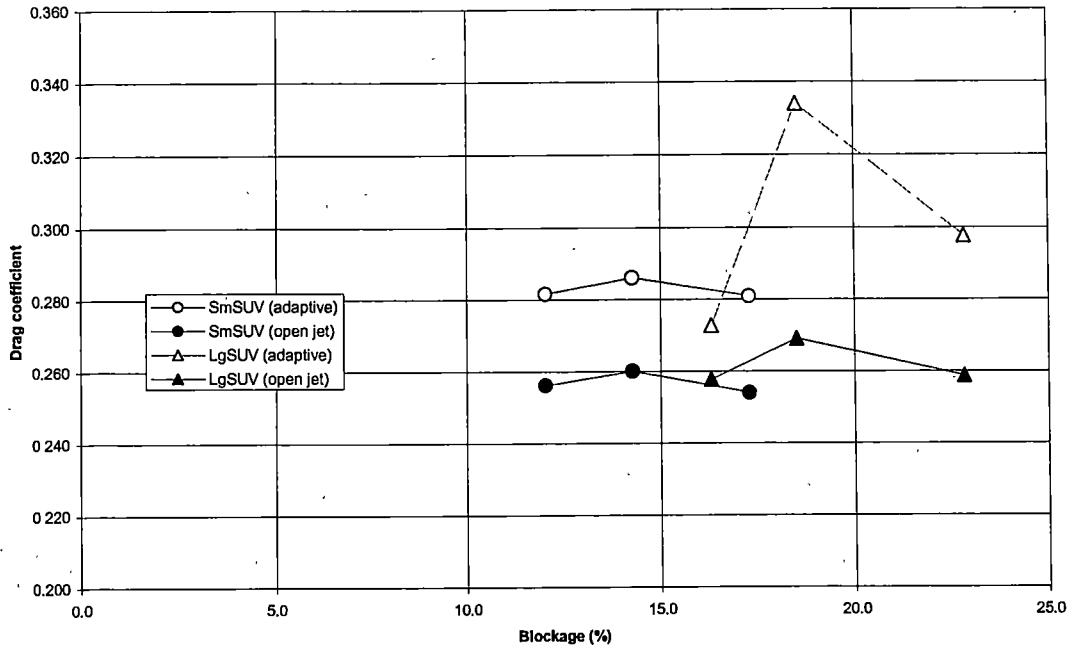


Figure 34.  $C_D$  values for the SUV models.

The Large SUV-Medium Top adaptive wall data point is suspiciously out of place on the plot, and may be erroneous. This is substantiated by the University of Maryland data shown Figure 35, which illustrates that this model has a higher  $C_D$  than the other Large SUV models. The Small SUV data are also consistent with this trend—showing a slightly higher  $C_D$  for the  $W/H=1.0$  SUV models.

Comparison is good between the adaptive wall and UMD data for the Sport Utility Vehicles. The trend of slightly higher  $C_D$  for the middle-height SUV models is still apparent in the UMD data. For purposes of making comparisons, the adaptive wall data are presented at the UMD blockages. Actual model blockages in the adaptive wall can be found in Appendix A.



Figure 35.  $C_D$  values for the SUV models (University of Maryland and adaptive wall).

The Large SUV-Medium Height appears out of place on the plot, suggesting that it is an anomaly of the experiment. However, the consistent offset between the UMD data and the adaptive wall data—likely caused by the removal of the “half-wheels”—is again present.

The SUV  $C_L$  values are shown in Figure 36. A notable feature of this figure is the increase in the difference between open jet and adaptive wall data as the model size increases. Recall that the aspect ratio of the SUVs is changing simultaneously with blockage. In fact, the model height is changing disproportionately with model blockage, unlike the MIRA models that changed at a constant rate with respect to model size. This feature may be linked to a jet deflection effect, which will be discussed in a later section.

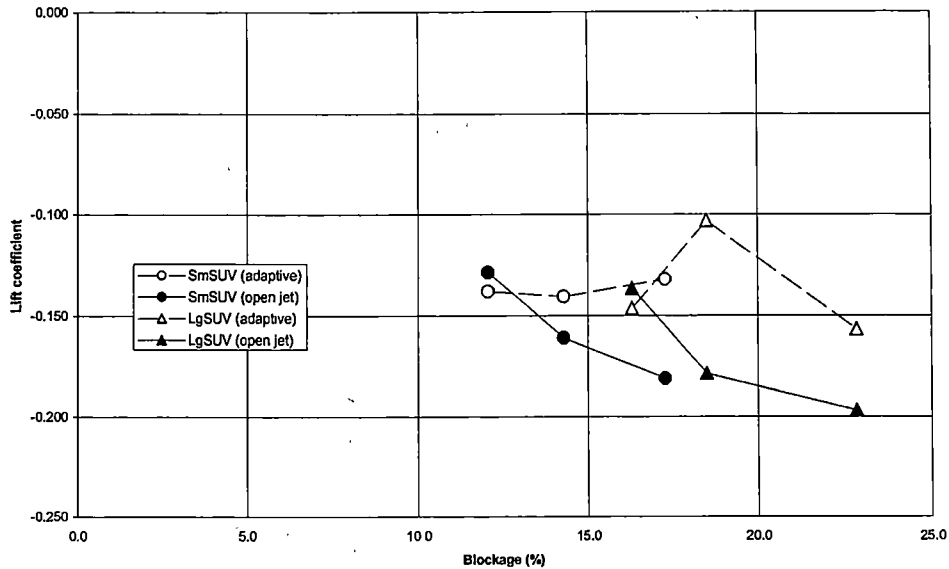


Figure 36.  $C_L$  values for the SUV models.

The Large SUV (medium height) model's  $C_L$  appears out of place when compared to the UMD data and the open jet data. The UMD data (found in Table 12) reveal a consistent  $C_L$  value for the SUV models, with slight differences due to the increasing height. This suggests that the  $C_L$  and  $C_D$  for the Large SUV (medium height) are irregularities caused by errors during the execution of the experiment.

#### Adaptive Wall: MIRA and SUV Models

The entire adaptive wall data set is presented in this section, from Figure 37 to Figure 53. Convergence was defined to have occurred when the most recent change of the test section wall contour resulted in a change in  $C_D$  of less than 1% relative to the previous iteration. This typically required up to 6 iterations, but some cases required fewer. The final wall shape from the previous model was used as the initial wall shape for the next model in all but one case, the MIRA 20 squareback (shown in Figure 45).

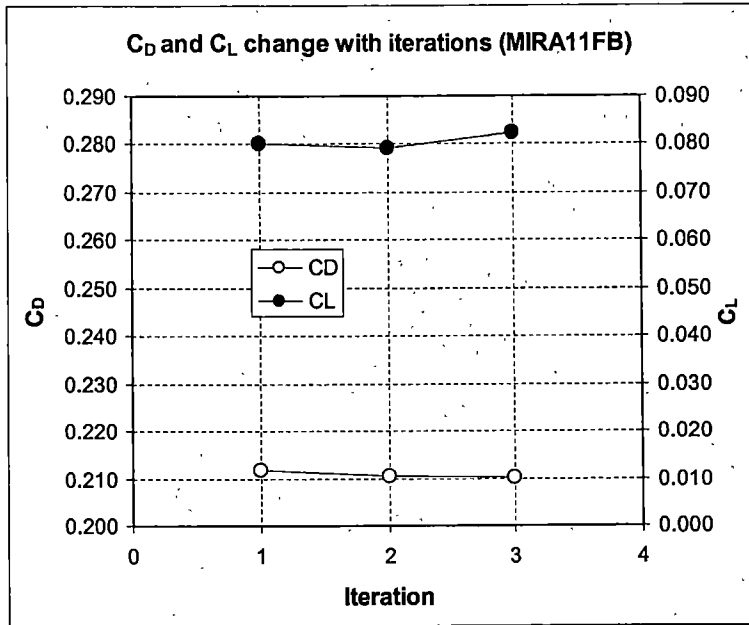


Figure 37. MIRA 11 Fastback.

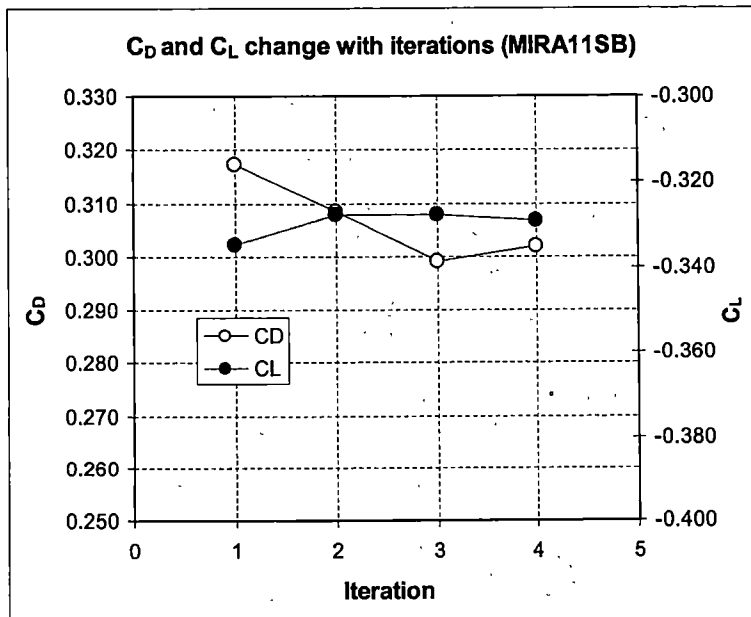


Figure 38. MIRA 11 Squareback.



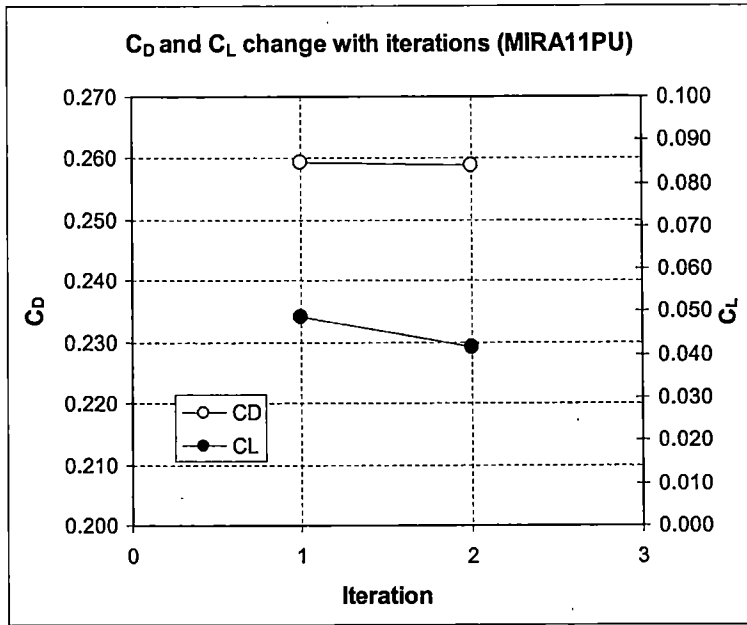


Figure 39. MIRA 11 Pickup.

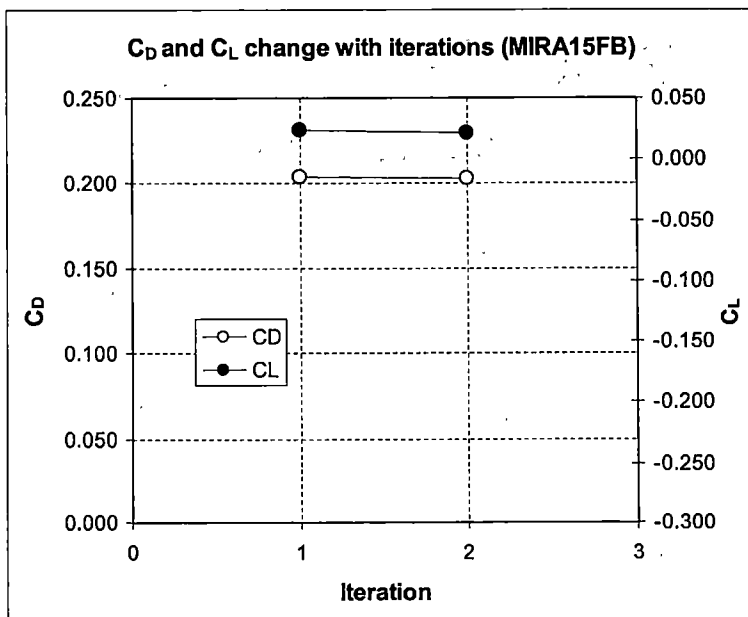


Figure 40. MIRA 15 Fastback.

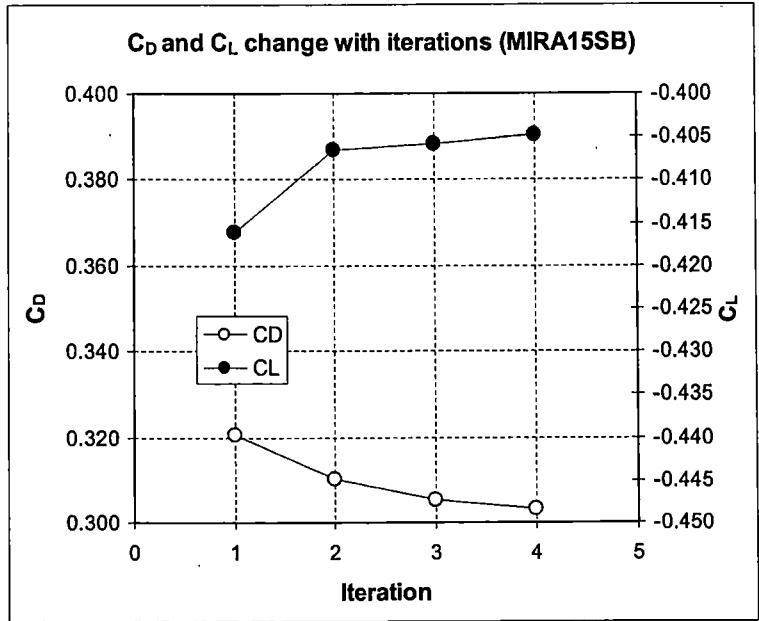


Figure 41. MIRA 15 Squareback.

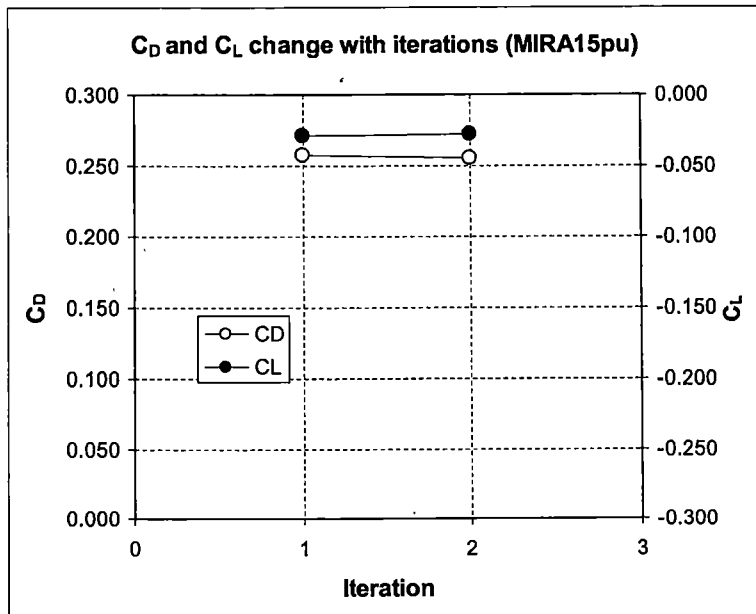


Figure 42. MIRA 15 Pickup.

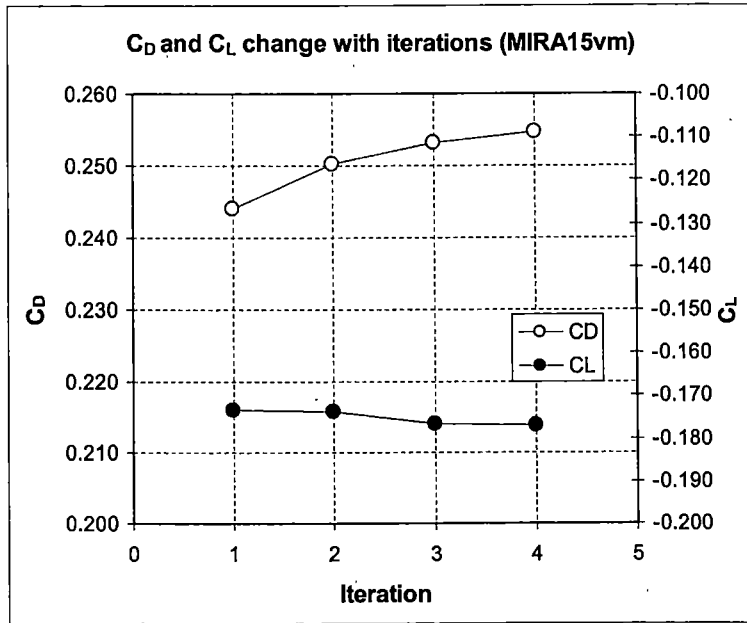


Figure 43. MIRA 15 Validation Model (Fastback with spoiler).

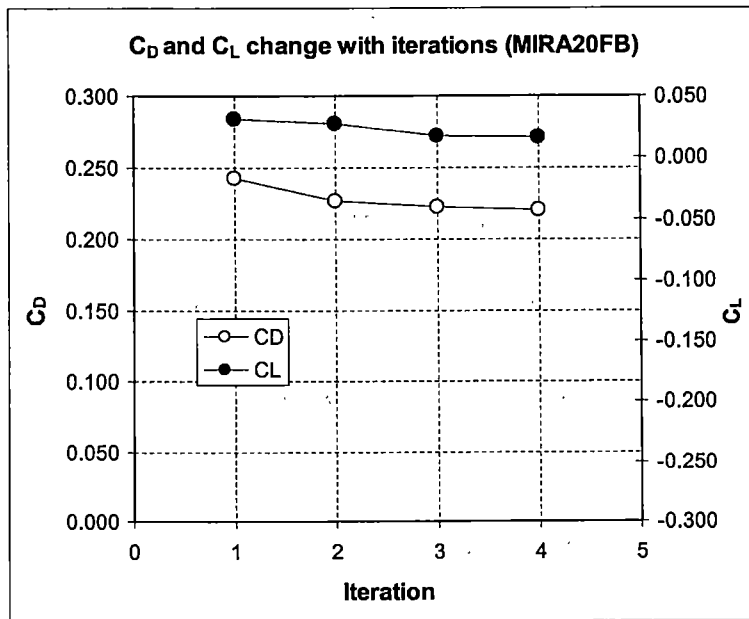


Figure 44. MIRA 20 Fastback.

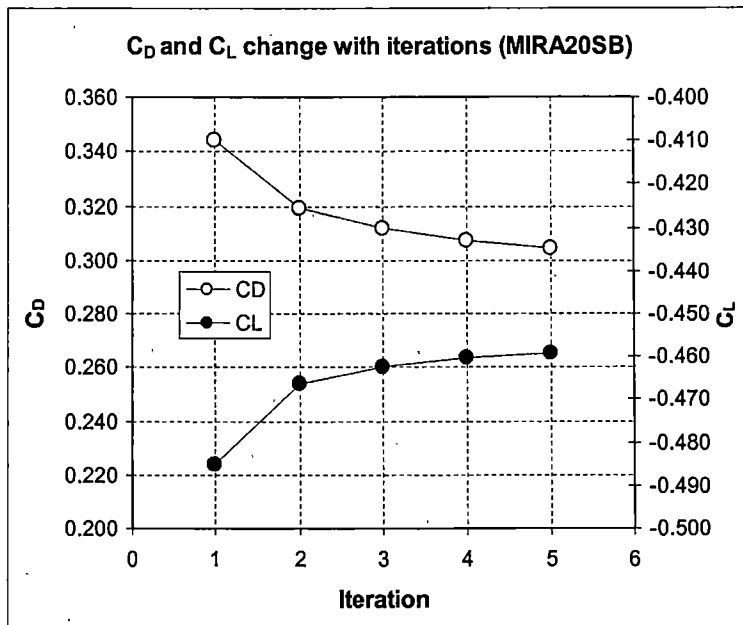


Figure 45. MIRA 20 Squareback.

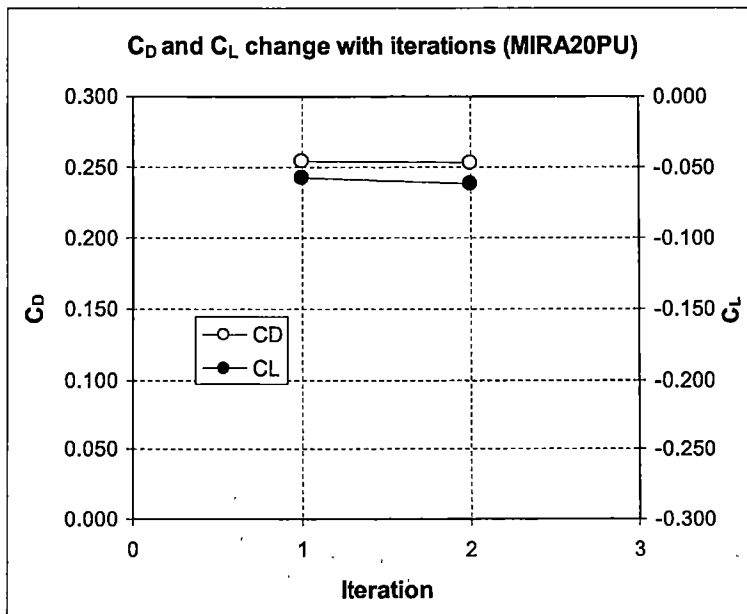


Figure 46. MIRA 20 Pickup.

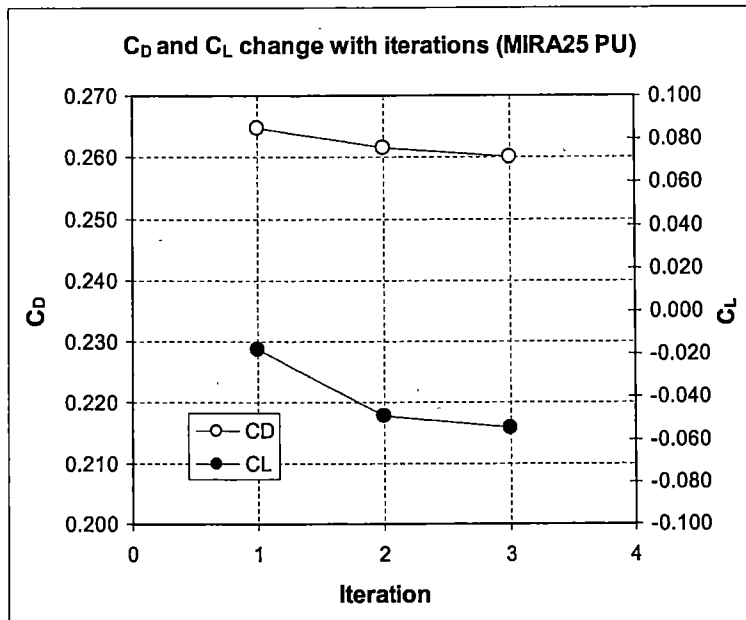


Figure 47. MIRA 25 Pickup.

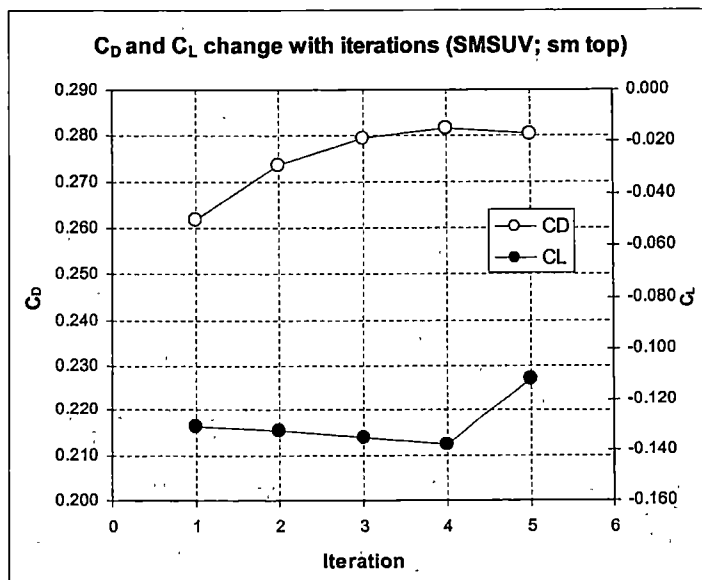
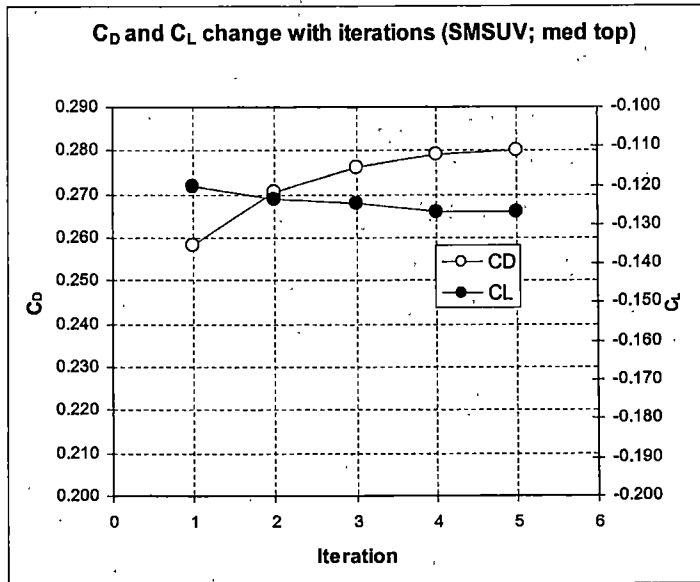
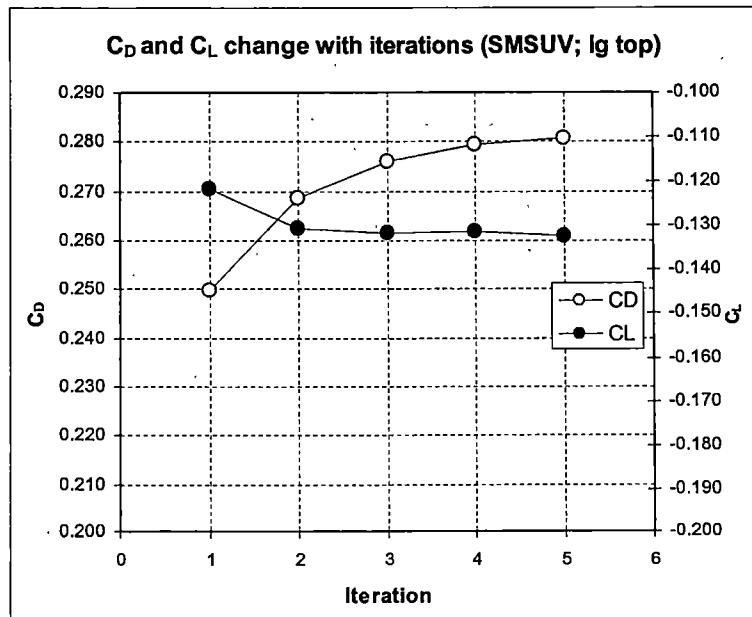


Figure 48. Small SUV (Low height).



**Figure 49. Small SUV (Medium height).**



**Figure 50. Small SUV (High height).**

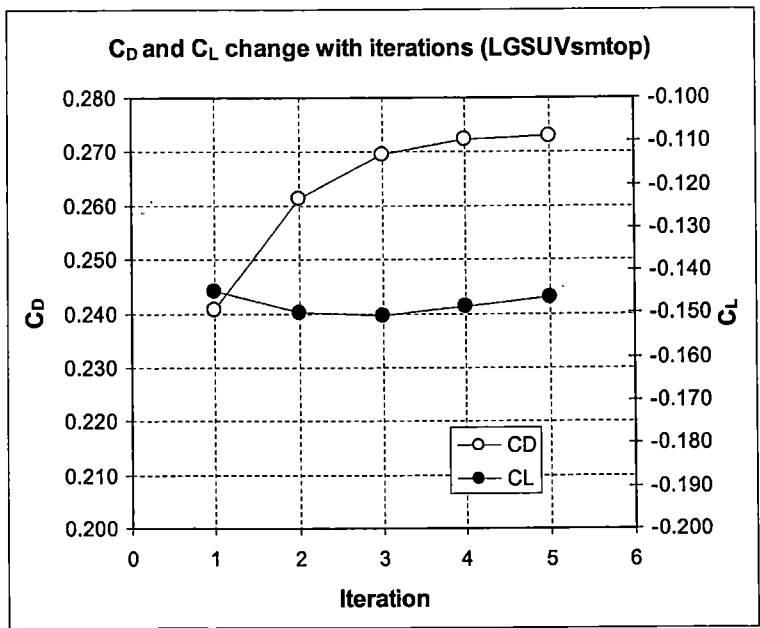


Figure 51. Large SUV (Low height).

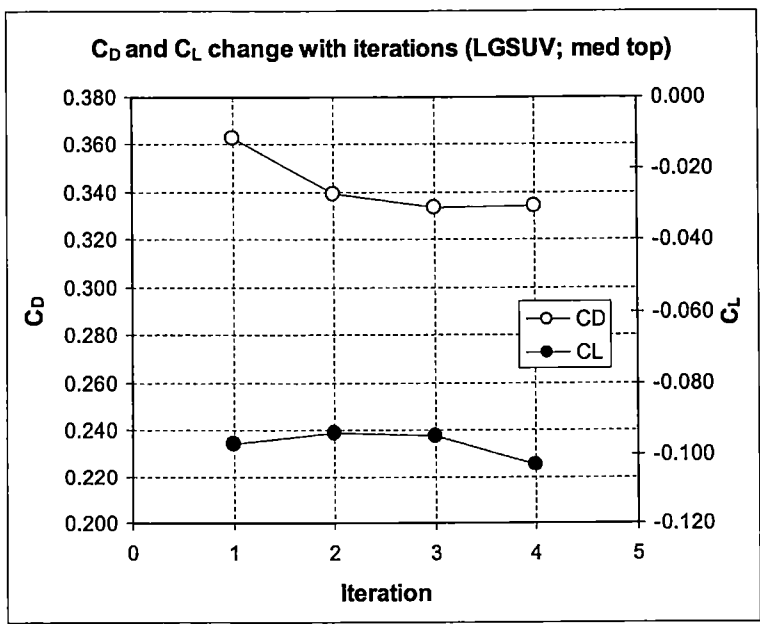
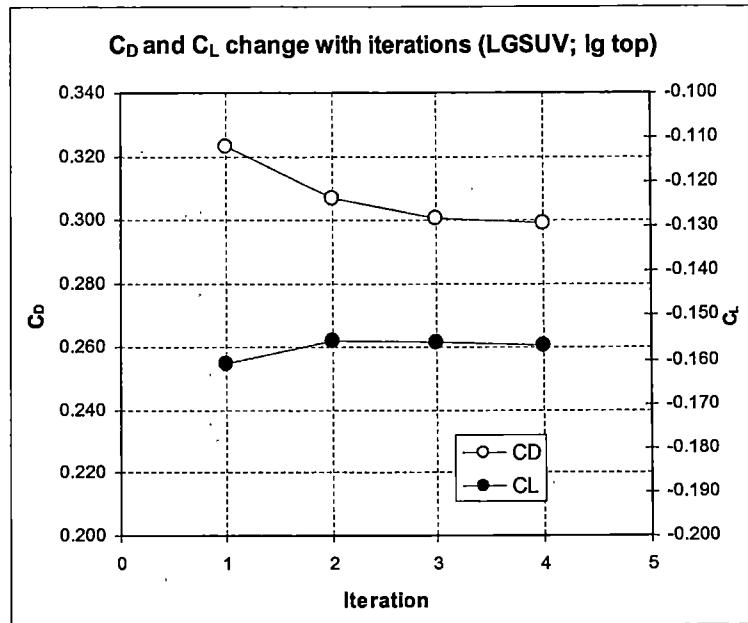


Figure 52. Large SUV (Medium height).



**Figure 53. Large SUV (High height).**

The adaptive wall plots illustrate the final result of each iteration, showing that the adaptive wall successfully converged in every case. In cases requiring a higher number of iterations, the initial wall positions were typically the converged wall positions for a model with very different geometry. In cases with few iterations, the previous model was likely similar in shape and/or size. Also, because some data points were acquired more than once (for repeatability checks), the wall shapes were well known and could therefore be set before the first iteration. In this scenario, usually only one iteration was required to verify that further wall changes would be such that there was no measurable effect on the data.

The data acquisition sequence was similar to that of the open jet. The model was installed at the correct height and a pre-test wind-off measurement taken. The correct



test speed was set, and the model sideforce was zeroed by adjusting the rotation stage on which the balance was mounted. This assured that the model axis was aligned with the flow. The first data set was taken, and a post-test wind off was acquired. At this point, the required wall movement was determined using the adaptive wall algorithm. This process was completed without disturbing the model. Model ground clearance was maintained at 1.07 inches for both adaptive wall and open jet tests in the model tunnel.

## Chapter 6

### Results of Regression Analysis

The lift and drag correction equations were developed using multivariate linear regression techniques and the data sets included in this report. All open jet and adaptive wall data were included in the regression analysis—with the lone exception of the validation model, which was held out of the analysis to serve as an independent “test case” for the resulting lift and drag corrections. All open jet aerodynamic coefficients used in the correlation were based on dynamic pressure measured using the nozzle method (as opposed to the plenum method).

Developing a linear lift or drag correction consists of assigning “weighting coefficients” to all of the independent variables under consideration. As the absolute value of an independent variable’s coefficient increases, the significance of the independent variable to the overall correction magnitude increases. The relative importance of the independent variables can be determined only by considering the coefficient-variable products, since the range of magnitudes varies for the different independent variables, e.g, 0.1 to 0.25 for blockage versus 0.9 to 1.5 for aspect ratio). The dimensionless independent variable values for each model are presented in Appendix A, Table 14.

The regression analyses were carried out with different combinations of independent variables to identify the least number of variables that would provide a suitable

correction. In so doing, the residual error from each variable combination gives a direct indication of which independent variables are important to the data correction process.

One fundamental decision was required with respect to the regression analysis. Since the correction was constrained to provide a lift (or drag) coefficient correction increment as a function of independent variables such as blockage, model geometry, and model position in the test section, one would expect that for a model with some ideal set of independent variables (e.g. zero blockage), the correction increment should go to zero, assuming no bias errors are present. This would imply that the constant "intercept" normally included in a linear equation should be constrained to be zero. Conversely, allowing the intercept to float to non-zero values provides the correction with an extra degree of freedom with which to minimize the residuals between the corrected open jet and adaptive wall results (given the constraint of a linear equation). In this study, both "zero intercept" and "floating intercept" correction equations were developed. For a given set of independent variables, the "floating intercept" models can be considered to represent an upper bound on the performance of the "zero intercept" models.

### **Drag correlation**

Each of the drag correlation equations included the open jet  $C_D$  as a standard variable. Additionally, blockage was included in all but one equation because of its well-established importance to aerodynamic simulation errors. The remaining equations used various combinations of the independent variables presented earlier. This permits a systematic comparison of the residual error obtained by using various groups of independent variables. As a point of comparison, blockage was *not* included in one case to verify that its inclusion was essential to minimize residual error.

*"Floating Intercept" Drag Corrections*

The values presented in Table 2 are the coefficients in the linear correlation equation that resulted from the regression analysis for the chosen independent variables, allowing a non-zero intercept. For example, the second line of Table 2 indicates a correction equation including  $C_D$ , blockage, and vehicle length/ $\sqrt{\text{Frontal area}}$ . This is presented in Equation 3

$$C_{D,Corrected} = 0.267 + 1.242 \cdot C_D - 0.279 \cdot \text{Blockage} - 0.089 \cdot \left( \frac{\text{Vehicle length}}{\sqrt{\text{Frontal area}}} \right)$$

**Equation 3**

**Table 2. Independent variables used in drag correlation.**

Intercept	$C_D$	Blockage	Vehicle Length / $\sqrt{\text{Frontal Area}}$	$\sqrt{\text{Frontal Area}}$ / Distance from nozzle to front bumper	$\sqrt{\text{Frontal Area}}$ / Distance from rear bumper to collector	Aspect ratio	Vehicle Height/Nozzle Height	Average error (%)	Maximum error (%)	Validation Model $C_D$ error (%)
-0.020	1.222	-0.116	-	-	-	-	-	4.6	18.5	2.6
0.267	1.242	-0.279	-0.089	-	-	-	-	2.4	12.7	0.8
-0.046	1.239	0.575	-	-0.091	-	-	-	3.0	13.0	2.5
0.190	1.249	2.187	-	-	-2.598	-	-	2.5	14.5	0.2
0.127	1.237	-0.234	-	-	-	-0.102	-	3.0	15.0	1.2
-0.106	1.253	-0.754	-	-	-	-	0.388	4.1	17.8	3.0
0.436	1.204	-	-0.078	-0.038	1.032	-0.114	-0.621	2.0	10.1	-0.2
0.396	1.197	1.797	0.010	-0.056	-0.413	-0.178	-0.797	1.9	10.6	-0.9

The average error resulting from applying this equation to the open jet data (and comparing those value to the adaptive wall results) is 2.4%. The maximum error is 12.7%, and the error between the corrected open jet  $C_D$  for the validation model and the adaptive wall  $C_D$  is 0.8%. In general, the error is reduced as more variables are included in the correction equation.

In general, Table 2 shows that the average error for the model ensemble does not vary substantially across the indicated sets of independent variables. Note that the average error is computed as the average  $C_D$  error as a fraction of the adaptive wall  $C_D$  over the model ensemble. The average errors in Figure 54 range from 2%-5%. Note that in Figure 54, the horizontal axis labels indicate the independent variables used to develop the specific correction equation.  $C_D$  was included as an independent variable in all of the cases. As an example, the second set of bars indicates the results for using a correction equation that includes  $C_{D, Open Jet}$ , *blockage*, and the ratio of *vehicle height/nozzle height*. The first set of bars represents the results of using a correlation equation that corrects raw open jet  $C_D$  values based only on *blockage*.

As also shown in Figure 54, the maximum error for any single model in the ensemble ranges from approximately 10%-20% for the various cases. On the surface, these results seem to suggest the selection of independent variables is somewhat arbitrary. However, bear in mind that the intercept was allowed to float. This provides an additional degree of freedom to the regression analysis that a forced-zero intercept equation does not have.

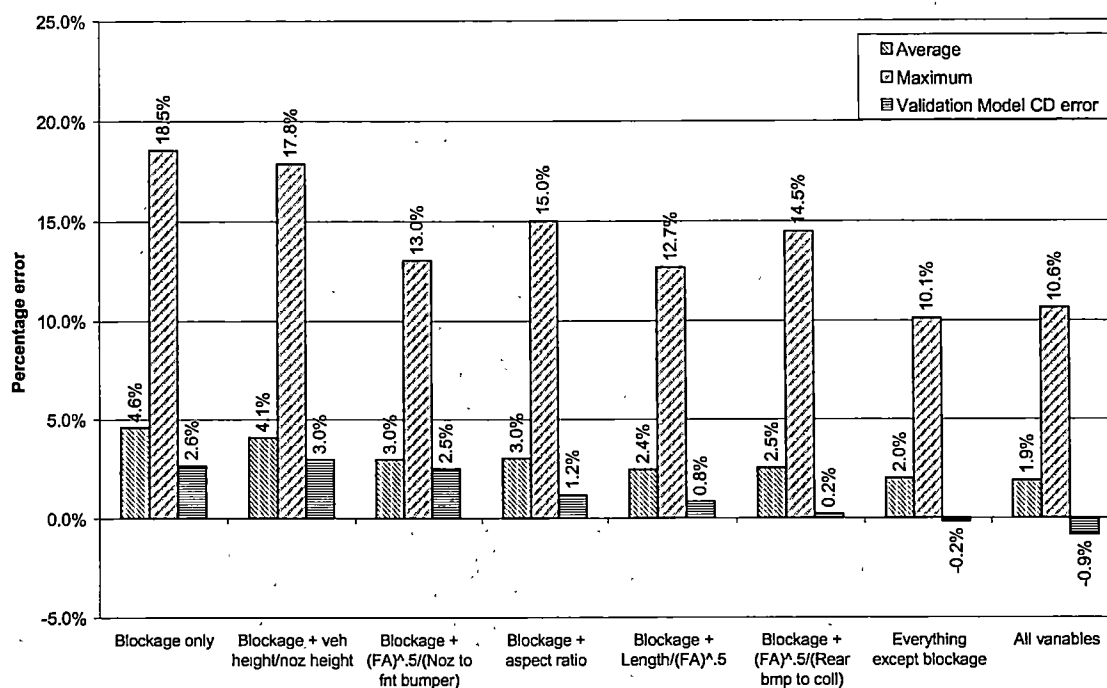


Figure 54. Errors from combinations of correlation variables ("Floating Intercept", Drag).

A simple thought exercise is instructive. If  $C_D$  is subtracted from each side of Equation 5, it becomes a formula for  $\Delta C_D$ . A non-zero intercept suggests that even if no correction increment is suggested from the independent variables (e.g.  $C_D = 0$ , Blockage = 0, etc.), a significant correction increment is indicated. This floating intercept explains the impressive results for the validation models, with errors in the range of 0%-3%.

In general, Figure 54 shows that increasing the number of independent variables in the correction equation reduces the error between the open jet and adaptive wall results. Each independent variable represents a degree of freedom for the regression, and simple mathematics dictate that increasing the degrees of freedom present in a system provides the system with more flexibility with which to minimize residuals. In addition, as

shown in Table 2, many of the correction equations suffer from a large intercept. From left to right on the plot, each variable is successively included with blockage (and raw  $C_D$ ) in the equation. The two sets of bars on the right-hand side of Figure 54 show the cases when "everything except blockage" and "all variables" are included in the correlation. These two cases yield the lowest average error.

Another way to quantify each parameter's importance is to examine the error with respect to the validation model. Because the validation model was not included in deriving any of the correlation equations, a small error is a strong positive indicator for the quality of a given correction equation. Figure 54 shows that two independent variable sets (plus intercept) results in small validation model errors: "blockage +  $\sqrt{\text{frontal area/distance from rear bumper to collector}}$ " and "everything except blockage". The latter seems counterintuitive due to the important role blockage plays in traditional correction schemes. However, another variable—namely the ratio of vehicle height to nozzle height—indirectly measures a vehicle's blockage by relating the vehicle and nozzle geometries. The former is a very encouraging result. Both model blockage and model-to-collector distance would be expected to be important independent variables.

Figure 54 also shows that there is a relatively large maximum error, regardless of the variables selected. This largest error always occurs with the Large SUV (medium top). Referring again to Figure 34, it can be seen that the drag coefficient for that vehicle appears to be an anomaly and is most likely due to experimental error. Including this point in the least squares regression forces the equation to fit to a point that is likely non-

physical. If you leave out the Large SUV (medium top) model, the maximum error is reduced to levels more consistent with the reported average error for each case.

The preferred drag correction equation is shown in Equation 4. It is chosen for its simplicity and for the accuracy with which it predicts the interference-free drag—employing only the frontal area and the vehicle's distance to the collector.

$$C_{D_{correct}} = 0.190 + 1.249 \cdot C_{D_{OJ}} + 2.187 \cdot Blockage - 2.598 \cdot \left( \frac{\sqrt{FrontalArea}}{rear\ bumper\ to\ collector} \right)$$

**Equation 4**

Table 3 shows the relative accuracy of the drag correlation equation for the various models in the ensemble using Equation 4. This table presents the predicted “interference-free”  $C_D$  value, the residual compared to the adaptive wall, and the error in percentage. It shows that even a modest set of independent variables can yield an accurate correction equation. From the standpoint of ease of application, this is in fact more desirable than an “all-inclusive” correction scheme that includes a large number of independent variables.

As stated in the discussion above, the Large SUV with the medium height exhibits the largest error when compared to the adaptive wall results. Although the error for each model obtained from each correction equation is not presented in this report, this same trend occurs regardless of the variable combinations employed; highlighting the fact that the drag results for this model are suspect.



**Table 3. Prediction accuracy of drag correlation equation using Equation 4.**

Model	$C_{D, Predicted}$	$C_{D, AW}$	% Error
Lg SUV (Lg)	0.309	0.298	3.50%
Lg SUV (Med)	0.292	0.334	15%
Lg SUV (Sm)	0.273	0.273	0.30%
MIRA 11 (FB)	0.216	0.21	2.60%
MIRA 11 (PU)	0.267	0.259	3.10%
MIRA 11 (SB)	0.307	0.302	1.60%
MIRA 15 (FB)	0.203	0.203	0.30%
MIRA 15 (PU)	0.255	0.255	0.10%
MIRA 15 (SB)	0.31	0.303	2.20%
MIRA 20 (FB)	0.219	0.22	0.80%
MIRA 20 (PU)	0.253	0.253	0.10%
MIRA 20 (SB)	0.311	0.304	2.10%
MIRA 25 (PU)	0.267	0.259	3.00%
Sm SUV (Lg)	0.286	0.281	1.70%
Sm SUV (Med)	0.282	0.286	1.40%
Sm SUV (Sm)	0.273	0.282	3.20%

The regression analysis was performed excluding this point, and the average error was recomputed. Using the same variable combination as in Equation 4, the maximum error reduces to 3.5% (from 14.5%), and the average error reduces to 1.3% (from 2.5%).

*“Zero Intercept” Drag Corrections*

The regression analysis was performed using the same combinations of variables as in the last section; however, the equation was forced to pass through zero. This forces the equations to obey a physically intuitive trend—going through zero when the parameters are zero. In the previous section, the curve fit was allowed to float, which could result in a non-zero coefficient even at zero blockages. The resulting linear coefficients are presented in Table 4, which has an identical format as Table 2.

**Table 4. Independent variables used in drag correlation.**

Intercept	$C_D$	Blockage	Vehicle Length / √Frontal Area	√Frontal Area / Distance from nozzle to front bumper	√Frontal Area / Distance from rear bumper to collector	Aspect ratio	Vehicle Height/Nozzle Height	Average error (%)	Maximum error (%)	Validation Model $C_D$ error (%)
0.000	1.146	-0.122	-	-	-	-	-	-0.2	18.8	3.0
0.000	1.412	-0.143	-0.022	-	-	-	-	4.0	16.3	1.3
0.000	1.073	0.519	-	-0.085	-	-	-	3.4	14.0	3.3
0.000	1.432	0.707	-	-	-0.913	-	-	3.9	16.2	0.8
0.000	1.419	-0.160	-	-	-	-0.050	-	3.7	16.0	1.0
0.000	1.039	-0.367	-	-	-	-	0.145	4.8	19.1	3.7
0.000	1.261	-	-0.009	-0.089	0.777	-0.043	-0.119	3.0	12.4	2.2
0.000	1.244	2.529	0.106	-0.108	-1.223	-0.143	-0.431	2.4	12.9	1.0

Consider the average error between the “floating intercept” and “zero intercept” corrections, found in Table 2 and Table 4, respectively. The first variable combination in the top row of both tables ( $C_D$  and blockage) yields a lower average error in the “zero intercept” case. The average error for the zero-intercept case is -0.2% versus 4.6% for the floating-intercept case. For all other combinations of independent variables, the floating-intercept case yields a smaller average error than the zero-intercept case. This general observation is not surprising given the additional degree of freedom for the floating-intercept regression. The error in drag correlation for the “zero intercept” case is graphically shown in Figure 55.

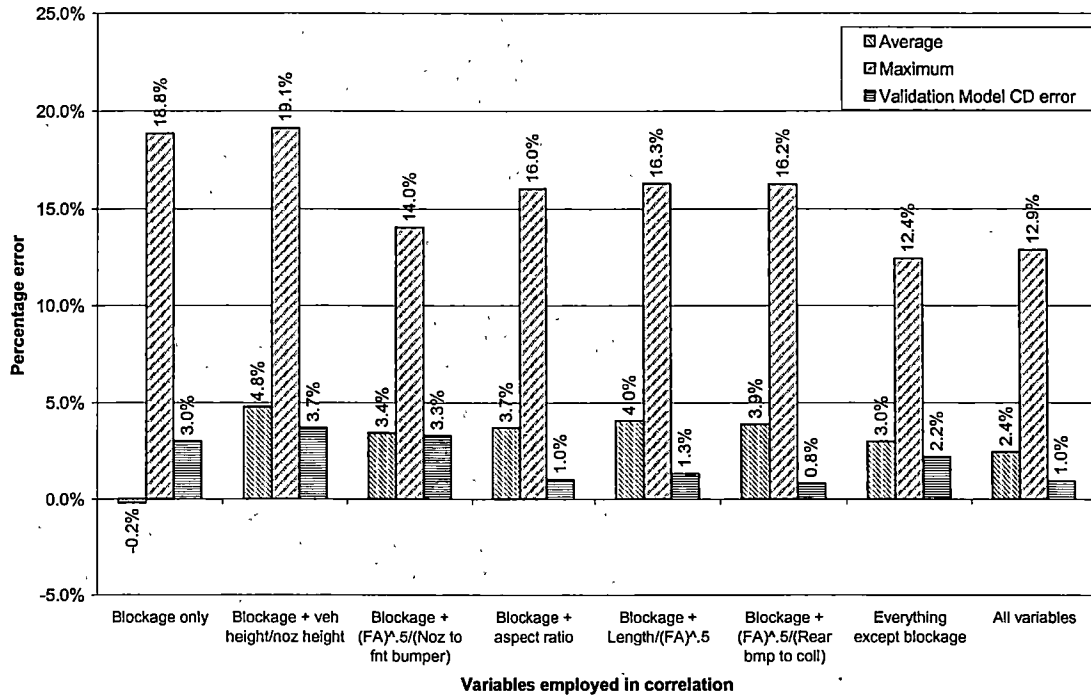


Figure 55. Errors from combinations of the correlation variables (“Zero Intercept”, Drag).

For consistency, the variables employed in the “floating intercept” case are also used here. While this aids in comparing the two different methods, the variables that minimize the error for the zero intercept case may be different. These variables are the vehicle blockage and the position-related parameter,  $\sqrt{\text{Frontal area}}/(\text{Distance from vehicle to collector})$ . Using the coefficients shown in Table 4, the resulting equation is shown in Equation 5:

$$C_{D_{correct}} = 0.000 + 1.432 \cdot C_{D_{OJ}} + 0.707 \cdot \text{Blockage} - 0.913 \cdot \left( \frac{\sqrt{\text{Frontal Area}}}{\text{Rear bumperto collector}} \right)$$

Equation 5

Table 5 presents the predicted drag coefficient using Equation 5, which employed a zero intercept approach. Direct comparison between the “zero intercept” and “floating intercept” techniques is possible. In general, the error in the “zero intercept” case is greater than the “floating intercept” approach. This indicates that the “floating intercept” approach is a more desirable technique to use because it provides a corrected coefficient that is closer to the interference-free value.

**Table 5. Prediction accuracy of drag correlation equation using Equation 5.**

Model	$C_{D,Predicted}$	$C_{D,AW}$	% Error
Lg SUV (Lg)	0.284	0.298	4.70%
Lg SUV (Med)	0.287	0.334	16%
Lg SUV (Sm)	0.275	0.273	0.90%
MIRA 11 (FB)	0.201	0.21	4.30%
MIRA 11 (PU)	0.260	0.259	0.60%
MIRA 11 (SB)	0.306	0.302	1.30%
MIRA 15 (FB)	0.197	0.203	3.40%
MIRA 15 (PU)	0.256	0.255	0.70%
MIRA 15 (SB)	0.320	0.303	5.20%
MIRA 20 (FB)	0.222	0.220	0.70%
MIRA 20 (PU)	0.261	0.253	3.30%
MIRA 20 (SB)	0.328	0.304	7.10%
MIRA 25 (PU)	0.281	0.259	7.90%
Sm SUV (Lg)	0.275	0.281	2.10%
Sm SUV (Med)	0.282	0.286	1.50%
Sm SUV (Sm)	0.276	0.282	2.00%

### Lift correlation

Lift correction equations are derived using the two methods described earlier: "floating intercept" and "zero intercept."

#### *"Floating intercept" Lift Corrections*

In the following section, the intercept was permitted to "float". The coefficients for the lift correlation equation presented in Table 6 take the same form as those for the drag correlation equations.

**Table 6. Potential variables used in lift correlation.**

Intercept	$C_L$	Blockage	Vehicle Length / √Frontal Area	√Frontal Area / Distance from nozzle to front bumper	√Frontal Area / Distance from rear bumper to collector	Aspect ratio	Vehicle Height/Nozzle Height	Average error (%)	Maximum error (%)	Validation Model Co error (%)
-0.079	-0.285	0.127	-	-	-	-	-	23.9	59.7	33.9
-0.316	-0.287	0.147	0.221	-	-	-	-	23.1	65.6	32.2
-0.050	-0.286	-0.008	-	0.108	-	-	-	21.8	63.8	33.9
-0.272	-0.288	-0.178	-	-	0.506	-	-	22.2	66.7	31.4
-0.161	-0.286	0.137	-	-	-	0.075	-	24.4	70.7	32.9
-0.055	-0.285	0.156	-	-	-	-	-0.053	24.5	67.9	34.1
-0.016	-0.285	-	0.107	0.213	-0.465	-0.058	0.265	19.0	57.0	35.4
0.108	-0.286	-0.798	-0.691	0.261	0.482	0.195	0.493	18.1	58.2	32.6

The same variables combinations are used to determine the relative effectiveness of each parameter. The average error is presented for each combination, as well as maximum error, and the error occurring when the correction is applied to the validation model. As would be expected, the average lift error decreases moderately as the complexity of the correction equation increases (i.e. the number of independent variables is increased). This is not consistent with the drag cases, where several combinations of few variables yielded relatively small errors. In fact, including more definition of the model/test section interaction may not be increasing the correlation's value at all. Rather, it may improve the correction because it is obtaining an improved fit to the original data set. Therefore, additional value may be extracted from the lift results by examining not only the variable combinations and regression analysis, but also the data trends seen between the open jet and adaptive wall tests.

Reexamining the MIRA lift results shown in Figure 32, we see that although lift coefficient becomes more negative with increasing model blockage, the adaptive wall results follow that trend closely. This trend is evident in the squareback, pickup, and fastback data.

The lift data reveal that increasing vehicle height may increase the amount of interference on lift. Observe in Figure 32 that the lift coefficient for the MIRA models measured in the open jet is nearly identical to the adaptive wall lift measurements. This is not true for the SUV models, as shown in Figure 36. For these models, the difference between open jet and adaptive wall  $C_L$  increases with increasing blockage. With regard to the model shapes, note that the SUV models increase only in height, whereas the

MIRA models increase in width and height proportionately. It can be speculated, then, that for a given width, a taller vehicle will experience interference effects causing more downforce. This is physically intuitive—a taller vehicle will tend to interfere more with the nozzle's top shear layer than a shorter vehicle. This interference might alter the static pressure on the upper surface of the vehicle, resulting in more downforce on the vehicle. This trend is consistent with the data. If this jet deflection effect dominates the lift measurements, it would be consistent with the findings of Mercker et al., which showed that the model's deflecting of the jet has a primary influence on test section aerodynamic interference (Mercker et al., 1996). The errors resulting from different combinations of the correlation variables ("floating intercept" for the lift data) are shown in Figure 56.

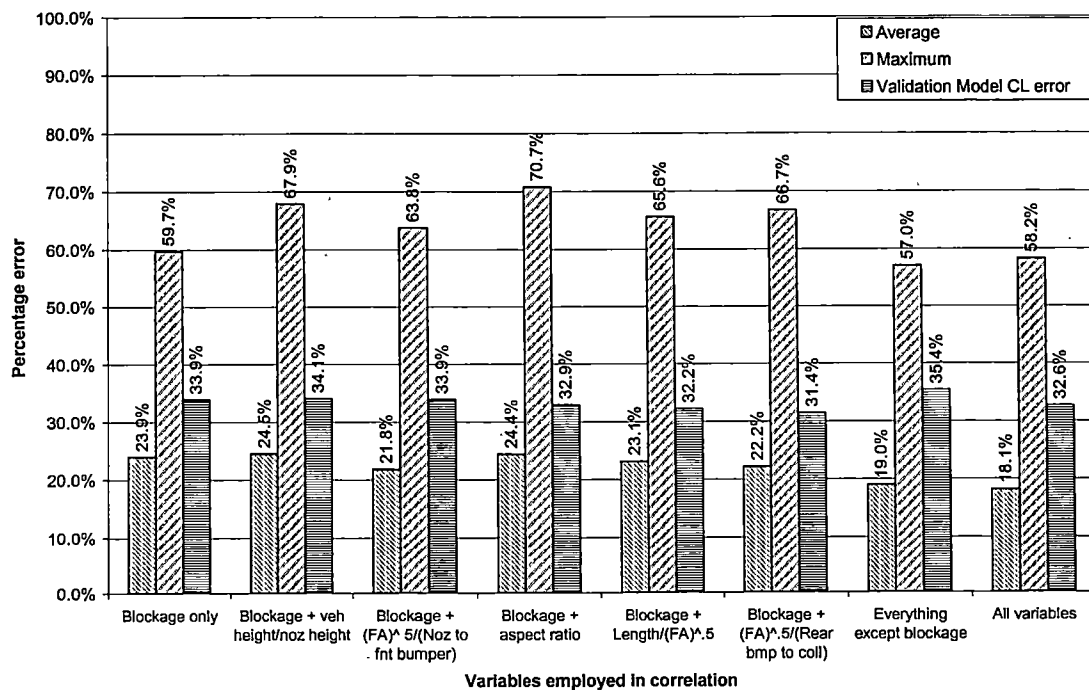


Figure 56. Errors from combinations of correlation variables ("Floating Intercept", Lift).

Equation 6 is the final correlation equation for vehicle lift coefficients measured in the subscale model of the employed open jet wind tunnel. As is the case with the drag correlation equation, the coefficients from Table 6 can be substituted into the equation.

$$C_{Lcorrect} = 0.108 + 1.117 \cdot C_{L,oj} - 5.360 \cdot Blockage - 0.225 \cdot \left( \frac{Length}{\sqrt{Frontal Area}} \right) + 0.290 \cdot \left( \frac{\sqrt{Frontal Area}}{Nozzle\ to\ front\ bumper} \right) \dots$$

$$\dots + 2.293 \cdot \left( \frac{\sqrt{Frontal Area}}{Rear\ bumper\ to\ collector} \right) + 0.146 \cdot Aspectratio + 1.105 \cdot \frac{Height_{Vehicle}}{Height_{Nozzle}}$$

**Equation 6**

Table 7 shows the relative accuracy of the lift correlation equation. This table presents the open jet lift coefficient, the adaptive wall lift coefficient (used as the reference), and the predicted "interference-free" value. Also presented is the error between the adaptive wall and predicted value of  $C_L$ . The difference between the corrected lift coefficient and that measured in the adaptive wall is also presented. This is because with measurements near zero, normalizing by that number creates large relative error values that do not communicate the absolute accuracy of the measurement.

#### *"Zero intercept" Lift Corrections*

The intercept was constrained to be zero in the following derivation of the lift correction equation. The results of this analysis are shown in Table 8. An obvious quality of the lift correction is its higher average errors. Keep in mind that the near-zero lift coefficients result in extremely high errors due to dividing by a number that is close to zero. The correction equation resulting from "everything except blockage" is an example where dividing by zero caused a tremendous error of over 6000%.



**Table 7. Accuracy of lift correlation equation with all variables (Floating intercept).**

Model	$C_{L,Predicted}$	$C_{L,AW}$	$\Delta C_L$	% Error
Lg SUV (Lg)	-0.153	-0.157	0.004	-3%
Lg SUV (Med)	-0.142	-0.103	-0.039	38%
Lg SUV (Sm)	-0.124	-0.146	0.022	-15%
MIRA 11 (FB)	0.097	0.082	0.015	18%
MIRA 11 (PU)	0.06	0.042	0.018	43%
MIRA 11 (SB)	-0.346	-0.329	-0.017	5%
MIRA 15 (FB)	0.005	0.021	-0.016	-75%
MIRA 15 (PU)	-0.051	-0.028	-0.023	84%
MIRA 15 (SB)	-0.41	-0.405	-0.005	1%
MIRA 20 (FB)	0.041	0.017	0.024	139%
MIRA 20 (PU)	-0.153	-0.157	0.004	-3%
MIRA 20 (SB)	-0.142	-0.103	-0.039	38%
MIRA 25 (PU)	-0.124	-0.146	0.022	-15%
Sm SUV (Lg)	0.097	0.082	0.015	18%
Sm SUV (Med)	0.06	0.042	0.018	43%
Sm SUV (Sm)	-0.346	-0.329	-0.017	5%

**Table 8. Potential variables used in lift correlation.**

Intercept	$C_L$	Blockage	Vehicle Length / $\sqrt{\text{Frontal Area}}$	Vehicle Distance from nozzle to front bumper	$\sqrt{\text{Frontal Area}} / \text{Distance from rear bumper to collector}$	Aspect ratio	Vehicle Height/Nozzle Height	Average error (%)	Maximum error (%)	Validation Model $C_D$ error (%)
0.000	1.114	0.403	-	-	-	-	-	29.0	69.0	27.0
0.000	1.113	0.750	-0.020	-	-	-	-	61.6	604.1	33.0
0.000	1.118	-0.518	-	0.148	-	-	-	31.7	114.8	30.2
0.000	1.112	1.425	-	-	-0.750	-	-	26.1	62.1	33.4
0.000	1.113	0.713	-	-	-	-0.043	-	25.9	60.2	33.4
0.000	1.114	1.364	-	-	-	-	-0.345	62.2	599.7	33.6
0.000	1.114	-	0.032	0.239	-2.129	-0.045	0.577	421.9	6465.2	35.5
0.000	1.118	-5.145	-0.197	0.275	2.002	0.152	1.198	29.9	210.4	31.9

The prediction of the validation model lift coefficient is used to compare the two techniques for deriving the lift correction equation. Both techniques yield very similar error values when predicting the validation model's lift coefficient. In fact, only in one case (the " $C_L$  and blockage" case) do the two vary significantly. In this case, the "zero intercept" scheme yields the lower error—consistent with earlier findings on  $C_D$ . This, again, is consistent with the primary physical process that dominates test section interference: blockage. The remaining variable combinations yield comparable estimates for  $C_L$  of the validation model, suggesting that neither technique is preferred in estimating lift.

It must be noted that deriving a correction equation for lift is difficult considering that measurement uncertainty was on the order of some results. That both approaches yield comparable errors may be an artifice of the large measurement uncertainty.

Figure 57 shows the average and maximum errors of the various correction equations resulting from a "zero intercept" approach. As can be seen from comparison with Figure 56, the maximum error is typically much smaller in the "floating intercept" approach than in the "zero intercept" case.

Table 9 presents the results of applying the "zero intercept" lift correction equation to the model set. The results are comparable to those shown in the "floating intercept" approach for the lift coefficient. For comparison, the  $\Delta C_L$  is also shown in the table.

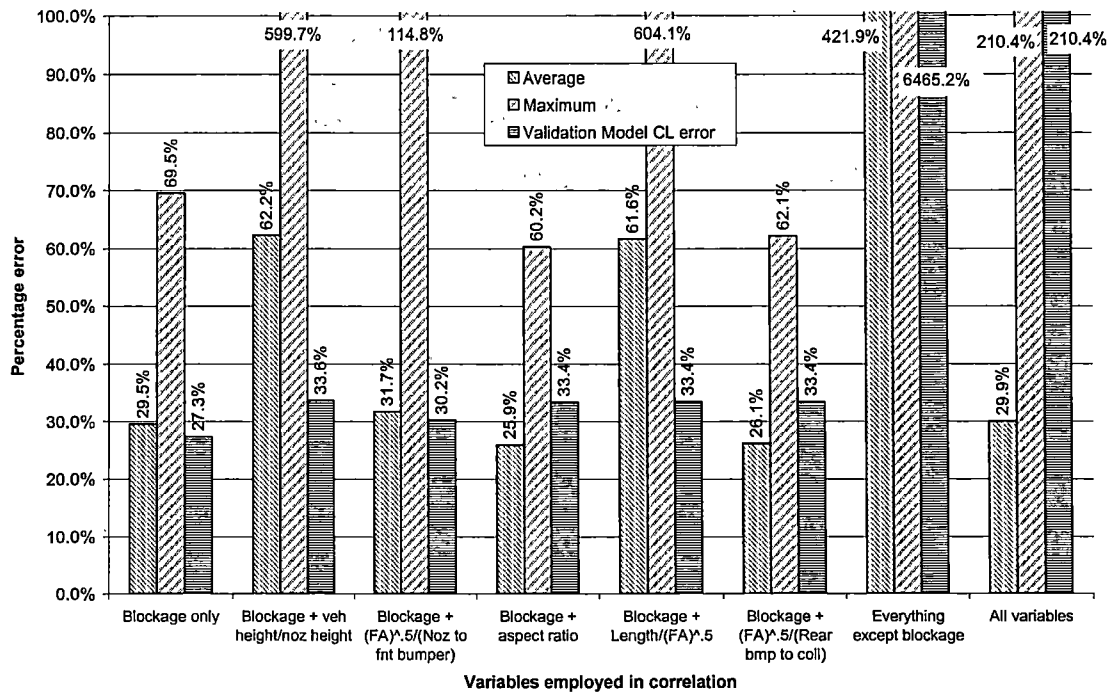


Figure 57. Errors from combinations of correlation variables ("Zero Intercept", Lift).

**Table 9. Prediction accuracy of lift correlation equation with all variables.**

Model	$C_{L, \text{Predicted}}$	$C_{L, \text{AW}}$	$\Delta C_L$	% Error
Lg SUV (Lg)	-0.152	-0.157	0.005	-3.00%
Lg SUV (Med)	-0.144	-0.103	-0.041	39.90%
Lg SUV (Sm)	-0.127	-0.146	0.019	-13%
MIRA 11 (FB)	0.096	0.082	0.014	17.20%
MIRA 11 (PU)	0.059	0.042	0.018	42.00%
MIRA 11 (SB)	-0.347	-0.329	-0.018	5.40%
MIRA 15 (FB)	0.007	0.021	-0.014	-68%
MIRA 15 (PU)	-0.05	-0.028	-0.022	78.50%
MIRA 15 (SB)	-0.409	-0.405	-0.004	0.90%
MIRA 20 (FB)	0.043	0.017	0.026	151%
MIRA 20 (PU)	-0.083	-0.157	-0.021	34.50%
MIRA 20 (SB)	-0.421	-0.103	0.039	-8.40%
MIRA 25 (PU)	-0.066	-0.146	-0.011	20.80%
Sm SUV (Lg)	-0.118	0.082	0.014	-11%
Sm SUV (Med)	-0.139	0.042	0.001	-1.00%
Sm SUV (Sm)	-0.142	-0.329	-0.004	2.70%

### Application of Correction to Validation Model

The lift and drag correction equations were applied to the validation model. Recall that the validation model data was not used in deriving the correlation to ensure that a completely independent verification would be accomplished. The result of this application of the correction equations is shown in Table 10, which shows that prediction of open jet interference using the derived correlation equation yields excellent agreement with the adaptive wall results. The lift prediction is less accurate for predicting open jet interference, as described earlier.

Table 11 shows the results of applying the "zero intercept" correction equations on the validation model. Comparison with the previous table shows similar results regardless of which approach is used (zero- versus floating-intercept). However, as mentioned earlier, an equation with several degrees of freedom is capable of fitting the data better due to its flexibility.

Measurement uncertainty can be estimated using the balance and load cell information stated earlier. For a  $C_D$  of 0.32 (typical for models employed here), the measurement uncertainty is 0.003, or 3 drag counts. Because the drag coefficients in the current study stay close to this value, measurement uncertainty for drag does not vary significantly from one model to the next.

**Table 10. Correlation accuracy for predicting  $C_D$  and  $C_L$  for validation model ("floating intercept" using all independent variables).**

	Open Jet	Adaptive Wall	Corrected	% Error
$C_D$	0.245	0.255	0.253	-0.9
$C_L$	-0.256	-0.177	-0.235	-33.9

Table 11. Correlation accuracy for predicting  $C_D$  and  $C_L$  for validation model ("zero intercept" using all independent variables).

	Open Jet	Adaptive Wall	Corrected	% Error
$C_D$	0.245	0.255	0.258	1.0
$C_L$	-0.256	-0.177	-0.233	31.9

Lift coefficient uncertainty is approximately 0.040, or 40 counts, using the result of Equation 2. For a squareback model, this represents an uncertainty of 13%. For a fastback with a spoiler, this represents an uncertainty of 30% or more. Fundamentally, the ability to minimize error in the lift corrections was limited by the uncertainty of the lift measurements, which is exacerbated by the fact that the models employed here have moderate downforce characteristics (i.e. the lift coefficients have small absolute values).

## Chapter 7

### Conclusion

Measurements were taken in subscale open jet and adaptive wall wind tunnels for the purpose of developing lift and drag corrections for open jet interference based on linear regression. The measurements yielded all six aerodynamic coefficients (three moments and three forces), but complete analysis has been performed on lift and drag only. Lift was measured using three load cells mounted to the balance employed in the previous tests. This arrangement has provided results consistent with the University of Maryland tests. Considering the lack of available lift results in model studies, the current tests have proven useful in understanding lift trends in open jets. The models employed range from 11% to 25% blockage in the open jet test section and characterize typical production vehicles.

Qualitatively, both the lift and drag results are consistent with trends shown in previous studies. The open jet drag coefficients increase with increasing blockage, as is commonly seen. These drag coefficients are below the reference (adaptive wall) value for blockages below 20%. The adaptive wall measurements yielded values for drag coefficient that were independent of vehicle blockage. These values are in agreement with the values obtained during the University of Maryland tests. The lift measurements yield consistent trends, as well. For example, the lift force on squareback models became more negative with increasing blockage. These squareback lift forces were

strongly negative—a trend that has been observed by other investigators. Measurements made at the University of Maryland were also included for confirmation of data trends.

The resulting correction equations minimize the effects of interference effects that naturally occur in open jet facilities. The linear regression model of the interference effects appears to be very effective in correcting for drag interference. Several of the drag correction equations presented in this report may be suitable for implementation at a full scale version of the wind tunnel modeled in the current study. However, the lift correction does not work as well. The ability to minimize error in the lift correction appears to have been fundamentally limited by the measurement uncertainty present in the lift measurements, which was amplified by the modest lift coefficients for the models employed in the study (large percentage uncertainty). However, lift trends with respect to blockage can be usefully extracted and applied in data corrections.

The current study provides a complete data set for predicting open jet drag and lift interference effects. Trends emerge from the data that can aid not only in the correction of interference effects in this subscale open jet model, but also in understanding open jet interference effects in general.

The ability to generate trustworthy reference data was a key element of the program. If the correction scheme is to adjust the open jet data to within acceptable tolerances for production testing (typically less than 1%), the experimental data from which the regression is derived must have accuracy that is of the same order. This further



indicates that the current data set can be used towards the development of a correction scheme appropriate for a full-scale facility, but its applicability is limited due to the relatively large uncertainty levels.

Future research of open jet interference can benefit from the author's experience in the current study. With that in mind, the following recommendations are offered. Revisiting the open jet and adaptive wall data with a semi-theoretical approach may provide a more solid understanding of the physical nature of the interference process. In the current work, the regression variables were selected based on engineering judgment and previous investigations. However, no theoretical derivation was performed to predict the relative importance of each of the parameters. Employing a semi-theoretical approach might offer more insight into the physical basis for open jet interference.

The author also recommends using a more accurate lift measurement. The transducers employed in the current study suffered from their relatively high uncertainty (1% of full-scale). Additionally, it is advised to use transducers with a maximum force input ranged for the expected loads.

Finally, employing additional dimensionless variables in the regression analysis may capture the complicated interferences within the test section more effectively. Such variables might take into consideration the empty test section flow quality, the vehicle aerodynamics, or further specify the geometrical relationship between the test article and the test section.

## Bibliography

## Bibliography

Aerodynamic Testing of Road Vehicles in Open Jet Wind Tunnels. SP-1465, Society of Automotive Engineers, Inc. (SAE), May 1999.

Ahmadi, M., Garry, K. P., "Preliminary Investigation of the Influence of a Ground-Plane Boundary Layer on the Aerodynamic Characteristics of Road Vehicle Models Tested Over a Fixed Ground," SAE Paper 96-0675.

Arnette, S.A.; Martindale, W.R.; "Advances in Wind Tunnel Aerodynamics for Motorsport Testing". SAE Paper 2001-01-3549.

Garry, K.P.; Cooper, K.R.; Fediw, A.; Wallis, S.B.; Wilsden, D.J. "The Effect on Aerodynamic Drag of the Longitudinal Position of a Road Vehicle Model in a Wind Tunnel Test Section," SAE Paper 94-0416.

Gilhaus, A., "The Main Parameters Determining the Aerodynamic Drag of Buses," *Colloque Construire avec le vent*, Vol. 2, Centre Scientifique et Technique du Batiment, Nantes, June 1981.

Goekna, L.N.; Varner, M.O.; "Studies Supporting the Development of an Automotive Adaptive-Wall Wind Tunnel". SAE Paper 90-0320, 1990.

Hackett, J.E., Wilsden, D.J., "Estimation of Wind Tunnel Blockage from Wall Pressure Signatures," AIAA Paper 78-828, April 1978.

Hoffman, J.; Martindale, B.; Arnette, S.; Williams, J.; Wallis, S. "Effect of Test Section Configuration on Aerodynamic Drag Measurements" SAE Paper 2001-01-0631.

Hucho, Wolf-Heinrich, Aerodynamics of Road Vehicles 4<sup>th</sup> Edition, SAE, 1998.

Kuentner R.; Deutenbach, K-R.; Vagt, J-D.; "Measurement of Reference Dynamic Pressure in Open-Jet Automotive Wind Tunnels". SAE Paper 920344.

Mercker, E.; Wiedemann, J. "On the Correction of interference Effects in Open Jet Wind Tunnels" SAE 960671.

Mercker, E., Wickern, G., Wiedemann, J., "Contemplation of Nozzle Blockage in Open Jet Wind Tunnels in View of Different 'Q' Determination Techniques," SAE SP-1232, February 1997.

Surface Vehicle Information Report: Aerodynamic Testing of Road Vehicles – Open Throat Wind Tunnel Adjustment. J2071, Published 1994 by SAE.

Wallis, S.; Williams, J., Personal communication between Hoffman, Wallis, and Williams on March 15, 2001.

Whitfield, J.D.; Jacocks, J.L.; Dietz, W.E.; Pate, S.R. "Demonstration of the Adaptive Wall Concept Applied to an Automotive Wind Tunnel". SAE Paper 82-0584, 1982.

Williams J.; Barlow, J.; Diaz, H.; Ranzenbach, R. "Experimental Study of  $C_D$  Variation With "Vehicle" Aspect Ratio", SAE Paper 1999-01-0649.

Wuest, W., Verdrängungskorrekturen für rechteckige Windkanäle bei verschiedenen Strahlbegrenzungen und bei exzentrischer Lage des Modells, Z. Flugwiss. 9, H. 1, 15-19 und H. 11, 362, Veiweg, Braunschweig 1961.

## Appendix

## Appendix A

### Tabulated numerical values for selected plots

#### Plotted values of $C_D$ and $C_L$

Table 12 presents the experimental data from the open jet and adaptive wall tests, and a partial listing of the University of Maryland data. Because such a large data set was taken at UMD—including variations of height, speed, and yaw—only the UMD data plotted within this document are shown here.

**Table 12. Numerical values for open jet, adaptive wall, and University of Maryland data.**

Model	Type	Adaptive Wall		Open Jet		University of Maryland	
		$C_D$	$C_L$	$C_D$	$C_L$	$C_D$	$C_L$
Mira 11	Fastback	0.210	0.082	0.201	0.060	0.220	-0.080
Mira 15	Fastback	0.203	0.021	0.203	-0.041	0.230	-0.122
Mira 20	Fastback	0.220	0.017	0.226	-0.047	0.246	-0.144
Mira 11	Pickup	0.259	0.042	0.242	0.027	0.277	-0.164
Mira 11	Squareback	0.302	-0.329	0.274	-0.336	0.319	-0.529
Mira 15	Squareback	0.303	-0.405	0.289	-0.413	0.319	-0.565
Mira 15	Pickup	0.255	-0.028	0.244	-0.092	0.276	-0.175
Mira 15	Validation model	0.255	-0.177	0.245	-0.256	-	-
Mira 25	Pickup	0.259	-0.055	0.272	-0.228	0.283	-0.192
Mira 25	Fastback	-	-	0.239	-0.166	0.250	-0.169
Mira 25	Squareback	-	-	0.320	-0.473	-	-
Mira 20	Pickup	0.253	-0.062	0.253	-0.159	0.272	-0.199
Mira 20	Squareback	0.304	-0.459	0.300	-0.461	0.314	-0.592
SmSUV	Low	0.282	-0.138	0.256	-0.129	0.325	-0.298
SmSUV	Med	0.286	-0.141	0.260	-0.161	0.333	-0.191
SmSUV	High	0.281	-0.132	0.254	-0.181	0.315	-0.102
LgSUV	Low	0.273	-0.146	0.258	-0.137	0.316	-0.191
LgSUV	Med	0.334	-0.103	0.269	-0.179	0.320	-0.163
LgSUV	High	0.298	-0.157	0.259	-0.197	0.309	-0.157

### **Model blockage**

Model blockage was different for different tunnels. Therefore, the Table 13 presents the model blockage for each model in each test section that was used. Note that all model geometries based on one MIRA model exhibit the same blockage.

Table 14 lists the dimensionless parameters for the various vehicle models used in the study. These values are presented to permit complete analysis using the coefficients for the correction equations found within the report.

**Table 13. Model blockage for all wind tunnels used in study.**

Vehicle Model*	Open jet test section	Adaptive Wall**	University of Maryland Wind Tunnel
MIRA 11 (All models)	11%	9%	0.21%
MIRA 15 (All models)	15%	12%	0.29%
MIRA 20 (All models)	20%	17%	0.39%
MIRA 25 (All models)	25%	21%	0.49%
Small SUV (Low height)	12%	10%	0.24%
Small SUV (Medium height)	14%	12%	0.28%
Small SUV (Large height)	17%	14%	0.34%
Large SUV (Low height)	16%	14%	0.32%
Large SUV (Medium height)	19%	15%	0.36%
Large SUV (Large height)	23%	19%	0.45%

\* : Blockages based on frontal areas including the "half-wheels" removed in the current study.

\*\* : Because test section area changed in the adaptive wall, blockage is based on the cross-sectional area of the contraction exit.

Table 14. Dimensionless parameters for models.

Model	Shape	Blockage	L/√FA	√FA/Noz to front bumper	√FA/Rear bumper to collector	Aspect Ratio	Vehicle height/Nozzle height
Lg SUV	lg top	22.9%	2.511	1.139	0.271	0.973	0.613
Lg SUV	med top	18.5%	2.789	1.025	0.244	1.176	0.507
Lg SUV	sm top	16.3%	2.974	0.962	0.229	1.388	0.429
MIRA11	FB	10.9%	3.069	0.637	0.179	1.336	0.382
MIRA11	PU	10.9%	3.069	0.637	0.179	1.336	0.382
MIRA11	SB	10.9%	3.069	0.637	0.179	1.336	0.382
MIRA15	FB	14.9%	3.069	0.900	0.218	1.336	0.446
MIRA15	PU	14.9%	3.069	0.900	0.218	1.336	0.446
MIRA15	SB	14.9%	3.069	0.900	0.218	1.336	0.446
MIRA15	VM	14.9%	3.069	0.900	0.218	1.336	0.446
MIRA20	FB	19.9%	3.070	1.344	0.265	1.336	0.515
MIRA20	PU	19.9%	3.070	1.344	0.265	1.336	0.515
MIRA20	SB	19.9%	3.070	1.344	0.265	1.336	0.515
MIRA25	PU	24.8%	3.069	2.019	0.310	1.336	0.576
Sm SUV	lg top	17.3%	2.692	0.898	0.231	0.991	0.537
Sm SUV	med top	14.3%	2.960	0.816	0.210	1.202	0.443
Sm SUV	sm top	12.1%	3.222	0.750	0.193	1.427	0.373



## Vita

Jeffrey Hoffman was born in Cleveland, Ohio on October 3, 1974. He attended St. Dominic Grade School and St. Ignatius High School in Cleveland before entering The University of Dayton. There, he majored in mechanical engineering and worked part-time as a research assistant in a low-speed wind tunnel laboratory where he conducted research using particle image velocimetry. He received the Bachelor of Science in Mechanical Engineering in 1998, and thereafter began employment with Sverdrup Technology, Inc., in Tullahoma, Tennessee. There he gained experience in the design of aerodynamic test facilities, concentrating on subscale model investigations and laser diagnostics. In addition, he led several wind tunnel commissioning programs for Formula One race teams, government-sponsored aerodynamic research institutes, and commercial automotive companies, taking him to several international jobsites.

He is presently an engineer and project manager at Sverdrup Technology in the Advanced Technology Segment.